Giuseppe Di Caprio

Quantitative label-free cell imaging by means of digital holographic microscopy: a roadmap for a complete characterization of biological samples

University of Naples "Federico II"

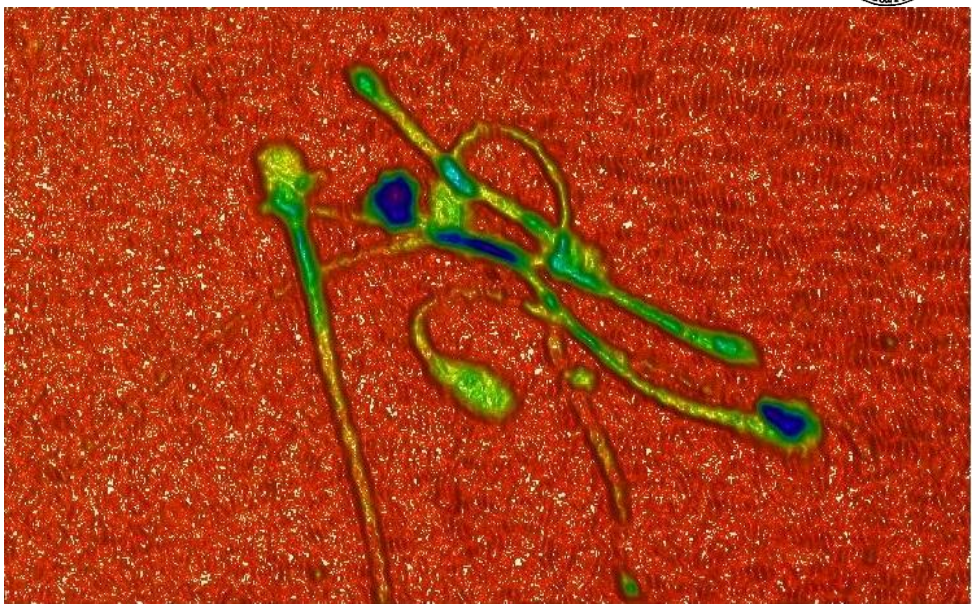

University of Naples "Federico II"

International PhD program
NOVEL TECHNOLOGIES FOR MATERIALS, SENSORS AND IMAGING
School of doctorate in Industrial Engineering

PHD THESIS

Quantitative Label-Free Cell Imaging by Means of Digital Holographic Microscopy: a Roadmap for a Complete Characterization of Biological Samples

Giuseppe Di Caprio

Supervisor:
Dr. Giuseppe Coppola
Institute of Microelectronics and Microsystems
National Council of Research

XXIV Cycle

Un infinito in atto non può essere pensato. Sicché un numero è infinito in potenza, ma non in atto. I matematici stessi, allo stato presente, non sentono il bisogno dell'infinito, bensì di una quantità grande quanto essi vogliono, ma pur sempre finita.

Aristotele, V sec. A.C.

L'anno prossimo vado in seconda, e so i numeri fino a quando finiscono.

Bambina su spiaggia, 2011 D.C.

SUMMARY

1. INTRODUCTION

1.1 A full characterization of biological samples: the technological challenge

In the last years, a big amount of work has been dedicated in numerous research fields in order to reduce the size of complex systems thus decreasing material and space requirements, achieving more efficient fabrication processes, lower costs and greater functionality. The rapid progress achieved in reducing the scale in the microelectronic and MicroEelectroMechanical System industries has created the opportunity to apply similar techniques to biological processing devices. However, nowadays, many of the systems used for visualizing biological samples are large benchtop systems that incorporate a variety of sensors, conventional optical microscope, complex fluid handling equipment, environment control systems, and bio-analysis tools. The cost of such equipment is usually high and the duration of performing multiple tests is relatively long. By reducing the size of the fluid networks to the micrometric scale, the length scale of the channel becomes comparable to the size of the materials to be analyzed. This provides potential for improved sensitivity of the system, drastic reduction in the time scales of diffusion and reaction, and high throughput by means of parallelization. However, the great interest in the developing of these microfluidic systems is not only for their potential low cost but for the possibility to achieve a label-free detection of single biological cells. This possibility is of broad interest in a variety of field, including clinical diagnostics, drug discovery, food safety, environmental monitoring and biological. This potentiality is considered a "hot topic" for a new industrial revolution, in fact many governments and companies are investing huge funds and the number of scientific publications is increasing exponentially (1), (2), (3). The characterization should be dedicated to a full description of the biological samples, thus containing static informations such as shape and thickness, and dynamical properties, such as velocity, linearity, wobble etc.

The research activity presented in this thesis has been mainly devoted to the analysis of bovine and human sperm cells. Sperm morphology is regarded as a significant prognostic factor for fertilization (4), as abnormal sperm morphology is one of the most common factors of male infertility. For this reason in the past years, several techniques have been developed in order to analyze, in greater detail, the morphological alterations of spermatozoa in their nearly physiological environment.

1.2 A review of the existing technique

For the monitoring of biological samples, physical parameters such as size, shape and refractive index are of crucial importance. Moreover, each biological sample is composed of many biomolecular ingredients such as lipids, sugars, proteins, nucleic acids and metabolites, whose concentrations are dependent on the types and states of the cells. Thus, most of the cells are inhomogeneous and so different parts of the cell may have different refractive indices. For example, the refractive index is normally 1.35-1.37 for cytoplasm, 1.38-1.47 for nucleus and 1.35-1.37 for extracellular fluid (5); thus, these structures are immersed in a fluid with a refractive index similar to that of the biological object under test. Most of the techniques commonly used to obtain such information involve biochemical processes that require specific laboratories and may alter the vitality of the sperm analyzed. On the other hand, spermatozoa appear essentially transparent under bright-field microscope, unless either optical-contrast interference microscopy (differential interference contrast (DIC) configuration) is used, or the specimen is stained and fixed (6): this type of microscope consists of an objective with a DIC configuration and an imaging lens to project a magnified image onto a person's retina or a CCD sensor. In addition to its relatively high implementation cost, the conventional microscope requires end-user expertise. Moreover the staining treatment reduces strongly the vitality of the cells making them useless for insemination (7). Finally, by optical microscopy, it is difficult and time-consuming to obtain a quantitative morphological imaging of the spermatozoa under test. In fact, a fine z-movement of the biological sample is required in order to acquire a collection of different planes in focus. This collection of acquired images is used in post-elaboration to produce a 3-D image

of the object under investigation. Some improvement can be achieved by using an atomic force microscopy (AFM) (8), (9) where the morphological information of the sample is obtained by raster scanning the sample under a sharp contact probe that is deflected by changes in sample thickness (z height). The position of the sample is adjusted to maintain a minimal set point deflection of the cantilever and these adjustments are used to generate a topographical map of the spermatozoa. However, the raster scanning could be timeconsuming limiting real-time characterization of the biological sample. Moreover, the cost of the technique makes its use in zootechnical industry not encouraging. The possibility to overcome these limitations and obtain a miniaturized version of the image-processing system is argument of relatively modern researches. In particular, Lange et al. (10) of the Stanford University have demonstrated the possibility to have a compact, on-chip imaging device with resolution around 10 microns. In this case, the biological specimen was placed directly on an image sensor, and the projection image is then recorded by the sensor. The main limitation of this configuration is relative to the resolution that is governed by the sensor's pitch size. Moreover, the systems is not sensible to the optical path variations. In 2006, Garcia-Sucerquia et al. (11) at the Dalhousie University in Canada, have demonstrated that it is possible to render microscope-resolution images of objects without the use of lenses. In this system an interferometric approach was used, so a tri-dimensional visualization of the objects was possible, however the developed system utilized macroscopic components. Finally, Psaltis's group (12), at the California Institute of Technology, has developed an on-chip optofluidic microscope, that consists of an opaque metal film with an etched array of submicron apertures and a microfluidic chip that is bonded onto the metal film. The configuration of this microscope allows to obtain a high-resolution acquired image, exploiting the time dimension during the image acquisition process. In particular, the specimen is raster-scanned over the array and the time varying transmissions of the light intensity through the afore-mentioned apertures are appropriately composed to obtain a well-defined image. However, in order to perform this procedure the speed and the morphology of the specimen must to be constant during the raster-scanning. This limitation can be a serious problem for the in-vivo

analysis of some biological samples, such as spermatozoa. Moreover, the described configuration returns a bi-dimensional variations of the image intensity, without any information about the morphology of the object under test. Actually, only the Garcia-Surcerquia's system allows to reconstruct a 3D shape of the biological specimens.

1.3 Skills and potentialities of Digital Holographic Microscopy

In the framework of the technological skills described in the latter paragraph, our research activity has been devoted to the setting up of a Digital Holographic Microscope, compatible with micro-manufactured devices (such as micro-channels), and to the development of the numerical algorithm aimed at the retrieval of the needed biological parameters.

In holographic interferometry, two or more wave fields are compared interferometrically, at least one of them must be holographically recorded and reconstructed. The method gives rise to interference patterns whose fringes are determined by the geometry of the holographic setup via the sensitivity vectors and by the optical path length differences. Thus holographic interference patterns can be produced by keeping the optical path length difference constant and changing the sensitivity vectors, by holding the sensitivity vectors constant and varying the optical path length differences, or by altering both of them between the object states to be compared. Especially the path lengths can be modified by a number of physical parameters. The flexibility and the precision gained by comparing the optical path length changes with the wavelength of the laser light used, make holographic interferometry an ideal means for measuring a manifold of physical quantities. The main advantages are:

- The measurements are contactless and noninvasive. In addition to an eventual loading for inducing the optical pathlength changes, the object is only impinged by light waves. The intensities of these waves are well below the level for causing any damage, even for the most delicate of biological objects.
- A reliable analysis can be performed at low loading intensities: the testing remains nondestructive.

- Not only may two states separated by a long time be compared, but furthermore the generation and evaluation of the holographic information can be separated both temporally and locally.
- Measurements can be made through transparent windows. We can therefore make measurements in pressure or vacuum chambers or protect against hostile environments. Due to the measurement of differences of the optical path lengths instead of absolute values, low quality windows do not disturb the results.
- Holographic interferometric measurements can be accomplished at moving surfaces: Short pulse illumination makes the method insensitive to a disturbing motion, vibrations can be investigated, the holographic setup can be made insensitive to specific motion components, and the rotation of spinning objects can be cancelled optically by using an image de-rotator.
- Deformation measurements can be performed at rough, diffusely reflecting surfaces, which occur frequently in engineering. No specular reflection of the object is required.
- The objects to be examined holographically may be of almost arbitrary shape. Using multiple illumination and observation directions or fiber optics, barely accessible areas can be studied.
- Holographic interferometry is nearly independent of the state of matter: Deformations of hard and soft materials can be measured. Refractive index variations in solids, fluids, gases and even plasmas can be determined.
- Lateral dimensions of the examined subjects may range from a few millimeters to several meters.
- The measurement range extends roughly speaking from a hundredth to several hundreds of a wavelength, for example displacements can be measured from about 0.005 μm to 500 μm.
- The achievable resolution and accuracy of a holographic interferometric displacement measurement permit subsequent numerical strain and stress calculations.
- Two-dimensional spatially continuous information is obtained: local singularities, for example local deformation extrema, cannot go undetected.

• Multiple viewing directions using a single hologram are possible, enabling the application of computerized tomography to obtain three-dimensional fields.

2. PRINCIPLES OF HOLOGRAPHY

In this chapter the physical basis of holography and holographic interferometry are discussed. The main phenomena constituting holography are interference and diffraction, due to the wave nature of light. A description of the wave theory of light as far as it is required to understand the recording and reconstruction of holograms and the effect of holographic interferometry is presented. In holographic interferometry the variation of a physical parameter is measured by its influence on the phase of an optical wave field. Therefore the dependence of the phase upon the geometry of the optical setup and the different parameters to be measured is outlined.

2.1 Light waves

Light is a transverse, electromagnetic wave characterized by time-varying electric and magnetic fields. Since electromagnetic waves obey the Maxwell equations, the propagation of light is described by the wave equation which follows from the Maxwell equations. The wave equation for propagation of light in vacuum is

$$\nabla^2 E - \frac{1}{c^2}\frac{\partial^2 E}{\partial t^2} = 0 \qquad (2.1)$$

where $\boldsymbol{E}$ is the electric field strength, ∇^2 is the Laplace operator

$$\nabla^2 = \frac{\partial^2}{\partial x^2} + \frac{\partial^2}{\partial y^2} + \frac{\partial^2}{\partial z^2} \qquad (2.2)$$

(x, y, z) are spatial coordinates, t the temporal coordinate, the time, and c is the propagation speed of the wave. Transverse waves vibrate at right angles to the direction of propagation and so they must be described in vector notation. The wave may vibrate horizontally, vertically, or in any direction combined of these. Such effects are called polarization effects. Fortunately for most applications it is not necessary to use the full vectorial description of the fields, so we can assume a wave vibrating in a single plane. Such a wave is called plane polarized. For a plane polarized wave field propagating in the z-direction the scalar wave equation is sufficient

$$\frac{\partial^2 E}{\partial z^2} - \frac{1}{c^2}\frac{\partial^2 E}{\partial t^2} = 0. \qquad (2.3)$$

It is easy verified that

$$E(z,t) = f(z-ct) \qquad \text{or} \qquad E(z,t) = g(z+ct) \qquad (2.4)$$

are also solution of this equation, which means that the wave field retains its form during propagation. Due to linearity of (2.4)

$$E(z,t) = a\, f(z-ct) + b\, g(z+ct) \qquad (2.5)$$

are also solution to the wave equation. This *superimpotion principle* is valid for linear differential equations in general and thus for (2.4) also.

The most important solution of (2.4) is the *harmonic wave*, whose real notation is

$$E(z,t) = E_0 \cos(kz - \omega t + \varphi_0) \quad (2.6)$$

where E_0 is the real amplitude of the wave, the term (kz-ωt) the phase of the wave; if we have not the maximum amplitude at x = 0 and t = 0, the relative phase φ_0 is present. The wave number k is associated to the wavelength λ by the relation $k=2\pi/\lambda$, while the angular frequency ω corresponds to the frequency f of the light wave by $\omega = 2\pi f$. Frequency f and the wavelength λ are related by the speed of light $c = \lambda f$.

The vacuum wavelengths of visible light are in the range of *400 nm* (violet) to *780 nm* (deep red). The corresponding frequency range is $7.5\cdot10^{14}$ *Hz* to $3.8\cdot10^{14}$ *Hz*. Light sensors (human eye, photodiodes, CCD camera, etc.) are not able to detect such high frequencies. The only directly measurable quantity is the intensity defined as the time average of the square of the electrical field

$$I = \varepsilon_0 c \langle E^2 \rangle_t = \varepsilon_0 c \lim_{T\to\infty} \int_{-T}^{T} E^2 dt \qquad (2.7)$$

where $\langle\,\rangle_t$ means the time average over many light periods and $\varepsilon_0 c$ is a factor derived by the Maxwell equations, ε_0 being the vacuum permittivity. For a plane wave (2.6) the intensity value is

$$I = c\varepsilon_0 {E_0}^2 \langle \cos(kz - \omega t + \varphi_0) \rangle_t = \frac{1}{2} c\varepsilon_0 {E_0}^2. \quad (2.8)$$

In order to avoid the calculation intricacy due to the trigonometric formula, the complex exponential notation is introduced by means of the *Eulero's formula*

$$e^{\imath\alpha} = \cos\alpha + \imath \sin\alpha\,. \quad (2.9)$$

The (2.6) can be thus rewritten as

$$E(z,t) = E_0 Re\left[exp\left(\imath(kz - \omega t + \varphi_0)\right)\right] \quad (2.10)$$

where *Re* denotes the real part of the complex function. During the computation the *Re* can be omitted, taking into account that only the real part represents the physical wave. One of the main advantages of the complex representation is the possibility to factorize the spatial and the temporal part

$$E(z,t) = E_0 \exp(\imath\varphi) \exp(\imath\omega t). \quad (2.11)$$

In many calculation of optics only the spatial distribution of the wave is of interest, named *complex amplitude.*

$$A = a \exp(\imath\varphi). \quad (2.12)$$

The latter two equations are valid, not only for plane waves, but three-dimensional waves whose amplitude a and phase $\boldsymbol{\varphi}$ can be function of x, y and z. In complex calculation the intensity can be easily calculated, neglecting the factor $1/2\varepsilon_0 c$, through the relation $I=|A|^2$.

A *wavefront* refers to the spatial distribution of the constant phase surfaces, as these surfaces propagate. The wavefronts are normal to the direction of propagation. In the case of plane wave propagation, the wavefront are flat and orthogonal to the propagation direction for each given time t.

A waveform often used in optics (due to the Huygens principle, that will be defined in the following) is relative to the spherical waves. The wave equation can be described in polar coordinates (r, θ, ψ), transformed by $x=r$ sinθ cos ψ, $y=r$ sin θ sin ψ, z=$r$cos θ. Due to the spherical symmetry, a spherical wave is not dependent on θ and ψ. Then the scalar wave equation is

$$\frac{1}{r}\frac{\partial^2}{\partial z^2}(rE) - \frac{1}{c^2}\frac{\partial^2 E}{\partial t^2} = 0. \quad (2.13)$$

The solutions of main interest are the harmonic spherical waves

$$E(r,t) = \frac{E_0}{r} e^{-i(kr-\omega t+\varphi)}. \quad (2.14)$$

One observes that the amplitude E_0/r decreases proportionally to $1/r$. Furthermore at a long distance from the origin the spherical wave locally approximates a plane wave.

2.2 Interference

The superposition of two or more waves, named *interference*, is the basis of holography and holographic interferometry. Being $E_i(r,t)$ solutions of the wave equation, the superposition

$$E(r,t) = \sum_i E_i(r,t) \quad i = 1,2,\ldots \quad (2.15)$$

since the wave equation is a linear differential equation.

Let's consider in the following the superposition of two wave having the same wavelength, and frequencies and the same polarization direction. The last condition allows us to use the scalar formalism. The complex amplitude of the wave is given by

$$A_1(x,y,z) = a_1 \exp(i\varphi_1) \quad (2.16)$$

$$A_2(x,y,z) = a_2 \exp(i\varphi_2).$$

The whole complex amplitude is given by the sum of the individual amplitudes $A = A_1 + A_2$. The intensity thus becomes

$$\begin{aligned} I = |A_1 + A_2|^2 &= (A_1 + A_2)(A_1 + A_2)^* \quad (2.17) \\ &= {a_1}^2 + {a_2}^2 + 2a_1 a_2 \cos(\varphi_1 - \varphi_2) \\ &= I_1 + I_2 + 2\sqrt{I_1 I_2}\cos\Delta\varphi \end{aligned}$$

where I_1 and I_2 are the intensities of the two beams and $\Delta\varphi$ the difference between the two phases. Consequently the resulting intensity is given by the intensity of the two beams plus a space varying interference term $2\sqrt{I_1 I_2}\cos\Delta\varphi$ depending on the phase difference

between the waves. The intensity reaches its maximum when $\Delta\varphi = 2n\pi$ (*constructive interference*) and its minimum when $\Delta\varphi = (2n+1)\pi$ (*destructive interference*)for $n = 1,2, \ldots$. The integer n is the inference order. An interference pattern consists then of dark and bright fringes as a result of the constructive and destructive interference. Up to now we only have investigated parallelly polarized waves. The complementary situation consists of orthogonally polarized waves. In this case the only effect of the superposition is the addition of the intensities $I = I_1 + I_2$. The visibility of the interference pattern is defined by

$$V = \frac{I_{max} - I_{min}}{I_{max} + I_{min}}. \quad (2.18)$$

If two parallel polarized waves of the same intensity interfere, we have the maximal contrast of V = 1; we have minimal contrast V = 0 for incoherent superposition.

2.3 Coherence

The resulting intensity of two different sources, e. g. two electric light bulbs directed on a screen, is in general additive. Instead of dark and bright fringes as expected by Eq. (2.16) only a uniform brightness according to the sum of the individual intensities becomes visible. In order to generate interfere fringes the phases of the individual waves must be correlated in a special way . This correlation property is named coherence and is investigated in this chapter. Roughly speaking, coherence is the ability of light to interfere. The two aspects of coherence are the temporal and the spatial coherence. Temporal coherence describes the correlation of a wave with itself at different instants. Spatial coherence depicts the mutual correlation of different parts of the same wavefront.

2.3.1 Temporal coherence

Temporal coherence describes the correlation of a wave with itself considering its behavior at different time instants (13) (14). To better afford this definition, let's introduce the Michelson's interferometer, showed in Figure 2.1. A light source is splitted by the beam splitter BS, the two resulting beams are back-reflected by the mirrors M1 and M2,

and superimpose on a screen. The two beams are usually not travelling exactly on the same direction but are slightly angled. On the screen a two-dimensional interference pattern is visible.

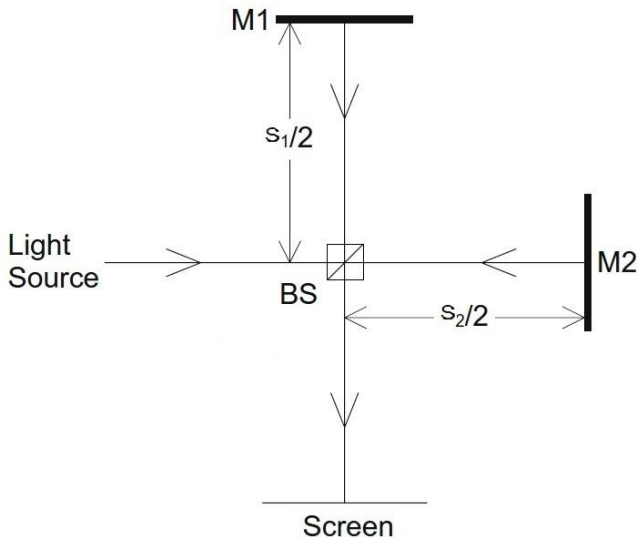

Figure 2.1 Michelson's interferometer

The optical path experienced by the two beams is respectively s_1 and s_2. In the experiment we can easily verify that the inference occurs only if the difference s_1- s_2 does not exceed a certain length L, otherwise the inference pattern disappears and the resulting intensity showed will be the addiction of the incoming beams. This is due to the fact that interference fringes can only appear if the two waves have a well-defined (constant) phase relation. In fact the phase difference between waves emitted by independent sources varies randomly thus preventing the interference. The atoms of the light source emit wave trains with finite length L. If the optical path difference exceeds this wave train length, the partial waves belonging together do not overlap on the screen and interference is not possible. This critical path length

difference or, equivalently, the length of a wave train is named *coherence length* L. The corresponding emission time for the wave train is the time of coherence $\tau = L/c$ is called *coherence time*.

By means of the formalism of Fourier a relation between the spectral width Δf and the coherence length can be found

$$L = \frac{c}{\Delta f} \ . \quad (2.19)$$

Light having a long coherence length is named highly monochromatic. The coherence length is then a measure for the spectral width. The length of coherence of thermal light e.g. light bulbs is of the order of micrometers while some laser used for research aims have coherence light of hundredth of kilometers.

Using equations (2.16) and (2.17) the visibility can be redefined, considering $\Delta\varphi = 0$ and $\Delta\varphi = \pi$ for I_{max} and I_{min} respectively, thus obtaining

$$V = \frac{2\sqrt{I_1 I_2}}{I_1 + I_2}. \quad (2.20)$$

In order to evaluate the self-coherence of E the following parameter is defined

$$\Gamma(\tau) = \langle E(t+\tau)E^*(t)\rangle = \lim_{T\to\infty} \frac{1}{2T}\int_{-T}^{T} E(t+\tau)E^*(t)dt \quad (2.21)$$

where $E(t)$ and $E(t+\tau)$ are the two partial waves of the interferometer delayed of a time τ. Can be thus defined the degree of coherence

$$\gamma = \frac{\Gamma(\tau)}{\Gamma(0)}. \quad (2.22)$$

Through simple calculation the (2.19) becomes

$$V = \frac{2\sqrt{I_1 I_2}}{I_1 + I_2}|\gamma| \quad (2.23)$$

and, for I_1=I_2

$$V = |\gamma|. \quad (2.24)$$

The degree of coherence in then related to the contrast of the fringe pattern and so to the ability of the two beams to interfere. $|\gamma|=1$ describes a monochromatic light i.e. a light with infinite length of coherence while $|\gamma|=0$ is related to a completely incoherent light. For a partially coherent light $0<|\gamma|<1$.

2.3.2 Spatial coherence

The mutual correlation of different parts of the same wavefront is described by the spatial coherence. To define this property the Young's interferometer, in Figure 2.2, can be used.

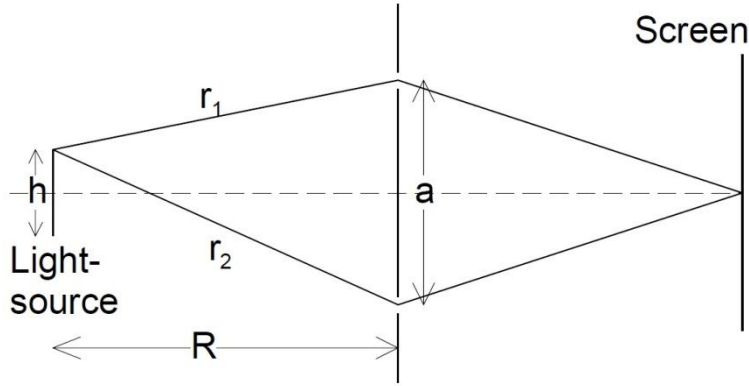

Figure 2.2 Young's interferometer

The light source is extended thus emitting light from different points. An aperture with two transparent holes is mounted between light source and screen. Under certain conditions, interference of the ray light coming from the upper and the lower hole are visible on the screen. The interference will be present if the distance between the holes will be keep lower than a critical limit, named coherence distance. This is due to the different optical path length for light rays emerging from different source points. Generally the contributions from all source points compensate themselves and the contrast vanishes. Nevertheless in some condition this compensation is avoided.

$$r_1 - r_2 < \frac{\lambda}{2}. \quad (2.25)$$

Being

$$r_1 = R^2 + \frac{(a-h)^2}{2} \;\; ; \;\; r_2 = R^2 + \frac{(a+h)^2}{2} \quad (2.26)$$

and using the assumption that a<<R and h<<R the (2.24) becomes

$$r_1 - r_2 \approx \frac{ah}{2R} \ll \frac{\lambda}{2}. \quad (2.27)$$

The coherence length a_k has then to fulfill the relation

$$\frac{\boldsymbol{a_k h}}{\boldsymbol{2R}} = \frac{\boldsymbol{\lambda}}{\boldsymbol{2}}. \quad (2.28)$$

The spatial coherence is thus not only a property of the light beam but it's depending on the geometry of the interferometer too. We can rewrite now the autocorrelation function in (2.20)

$$\Gamma(r_1, r_2, \tau) = \langle E(r_1, t+\tau) E^*(r_2, t) \rangle = \lim_{T\to\infty} \frac{1}{2T} \int_{-T}^{T} E(r_1, t+\tau) E^*(r_2, t) dt \quad (2.29)$$

r_1 and r_2 being the spatial vectors of the two holes. The normalized cross function is then

$$\gamma(r_1, r_2, \tau) = \frac{\Gamma(r_1, r_2, \tau)}{\sqrt{\Gamma(r_1, r_1, 0)\Gamma(r_2, r_2, 0)}} \quad (2.30)$$

being $\Gamma(\boldsymbol{r}_1,\boldsymbol{r}_1,0)$ and Γ $(\boldsymbol{r}_2, \boldsymbol{r}_2,0)$ the intensity at $\boldsymbol{r}_1$ and $\boldsymbol{r}_2$. $\gamma(\boldsymbol{r}_1,\boldsymbol{r}_2, \tau)$ describes the degree of correlation between the light field at $\boldsymbol{r}_1$ at time t+τ with the light field at $\boldsymbol{r}_2$ at time t. $\gamma(\boldsymbol{r}_1,\boldsymbol{r}_2, \tau$=0) measures the correlation between the field amplitudes at $\boldsymbol{r}_1$ and $\boldsymbol{r}_2$ at the same time and is named complex degree of coherence.

2.4 Diffraction

Let's consider a light wave which hits an obstacle. From geometrical optics it is known that the shadow becomes visible on a screen behind the obstacle. However this is not true in general. If the dimensions of the obstacle (e. g. diameter of holes in an opaque screen or size of

opaque particles in a transparent volume) are in the range of the wavelength, the light distribution forms a pattern of dark and bright regions. This phenomenon is named diffraction. The mechanisms of diffraction is of fundamental importance for understanding the principle of holography. A quantitative theory of diffraction is the eminent prerequisite, since we need a numerical rather than a qualitative approach. In this paragraph the main results of scalar diffraction theory as they are needed in what follows will be presented. The theory of diffraction is mainly based on the Huygens' principle:

Every point of a wavefront can be considered as a source point for secondary spherical waves. The wavefront at any other place is the coherent superposition of these secondary waves.

A graphical representation of the Huygens' principle is showed in Figure 2.3.

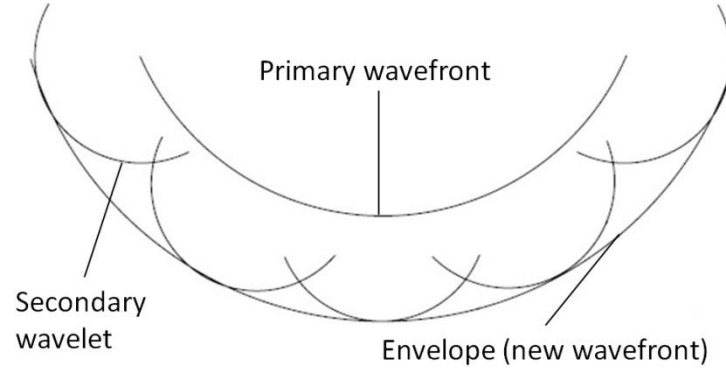

Figure 2.3 Huygens' principle

2.4.1 Fresnel-Kirkhhoff diffraction formula

The mathematical formulation of the Huygens' principle is given by the Fresnel-Kirkhhoff diffraction formula

$$\Gamma(\xi',\eta') = \frac{i}{\lambda}\iint_{-\infty}^{\infty} A(x,y)\frac{e^{-i\frac{2\pi}{\lambda}\rho'}}{\rho'}\mathcal{Q}\,dx\,dy \quad (2.31)$$

being

$$\rho' = \sqrt{(x-\xi)^2+(y-\eta)^2+d^2} \text{ and } \mathcal{Q} = \frac{1}{2}(\cos\theta + \cos\theta'). \quad (2.32)$$

The coordinate system defined in Figure 2.4. $A(x,y)$ is the complex amplitude in the plane of the bending aperture plane. $\Gamma(\xi',\eta')$ is the field in the observation plane (diffraction plane). While ρ' stands for the distance between a point in the aperture plane and a point in the observation plane.

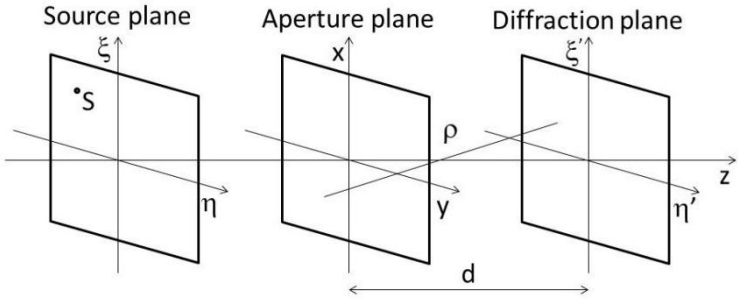

Figure 2.4 Coordinate system

The light source S in the source plane with coordinates (ξ,η) radiates spherical waves. The light is then propagated and $A(x,y)$ is the complex amplitude in the aperture plane. Let's consider an opaque aperture with only one hole at the position (x,y). This hole becomes now the source for secondary waves. The field at the position (ξ',η') of the diffraction plane is proportional to the field at the entrance side of the aperture $A(x,y)$ and to the propagated field of the secondary spherical wave emerging from (x,y), described by $\exp(-i\frac{2\pi}{\lambda}\rho')/\rho'$. Generalizing the aperture plane is regarded as a plane consisting of many sources for secondary wave. The resulting field in the diffraction plane is thus the integral over all secondary spherical waves, emerging from the aperture plane. According to the Huygens' principle the secondary waves can also propagate back into the direction of the source. Since this eventuality is not occurring in practice, the inclination factor $\boldsymbol{Q}$ defined in (2.31) is introduced in the Fresnel-Kirchhoff integral. $\boldsymbol{Q}$ depends on the angle θ between the incident ray from the source and the vector $\boldsymbol{n}$ perpendicular to the aperture plane, and on the angle θ' between the bended ray and $\boldsymbol{n}$, see Figure 2.5.

$\boldsymbol{Q}$ is approximately zero when $\theta \sim 0$ and $\theta \sim \pi$. This prevents waves travelling into the backward direction. In most practical situations the light beam is mainly propagating along the z direction and $\boldsymbol{Q} \sim 1$. The inclination factor can be introduced as an correction to the diffraction integral, as done here, or be derived analytically in the formal diffraction theory (14).

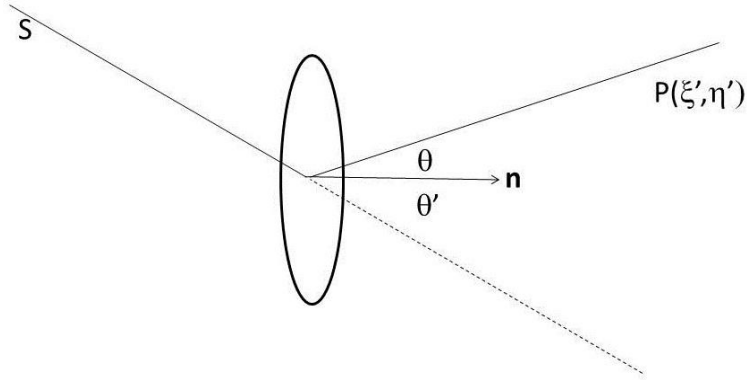

Figure 2.5 Angles

The sign in the argument of the exponential function of the Fresnel-Kirchhoff integral can be both positive both negative, depending on the definition of a harmonic wave in (2.10), However, using the "+" sign in Eq. (2.30) leads to the same expressions for all measurable quantities, as e.g. the intensity and the magnitude of the interference phase.

In the following the different approaches to solve the diffraction formula will be described, namely the Fresnel approximation, and the employment of the convolution theorem when propagation of light waves is viewed as a linear system.

2.5 Holography

A hologram is usually recorded on a photographic plate or a flat piece of film and produces a three-dimensional image. In addition, making a hologram does not involve recording an image in the conventional sense. In conventional imaging techniques, such as photography, what is recorded is merely the intensity distribution in the original scene. As

a result, all information about the optical paths to different parts of the scene is lost. The unique characteristic of holography is the idea of recording both the phase and the amplitude of the light waves from an object. Since all recording materials can record only the intensity in the image, it is necessary to convert the phase information into variations of intensity.

2.5.1 Hologram recording

By using coherent illumination and introducing, as shown in Figure 2.6, a reference beam derived from the same source, the hologram records both intensity and phase information. The photographic film records the interference pattern produced by this reference beam and the light waves scattered by the object.

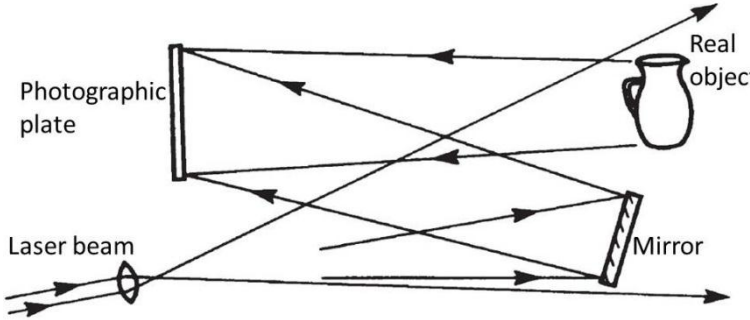

Figure 2.6 Hologram recording

Since the intensity at any point in this interference pattern also depends on the phase of the object wave, the resulting recording (the hologram) contains information on the phase as well as on the amplitude of the object wave. If the hologram is illuminated once again with the original reference wave, as shown in Figure 2.7, it reconstructs the original object wave. Therefore an observer looking through the hologram sees a perfect three-dimensional image. This image exhibits all the effects of perspective, and depth of focus when photographed, that characterized the original object.

In Gabor's historical demonstration of holographic imaging (15), a transparency consisting of opaque lines on a clear background as illuminated with a collimated beam of monochromatic light, and the

interference pattern produced by the directly transmitted beam (the reference wave) and the light scattered by the lines on the transparency was recorded on a photographic plate. When the hologram (a positive transparency made from this photographic negative) was illuminated with the original collimated beam, it produced two diffracted waves, one reconstructing an image of the object in its original location, and the other, with the same amplitude but the opposite phase, forming a second, conjugate image.

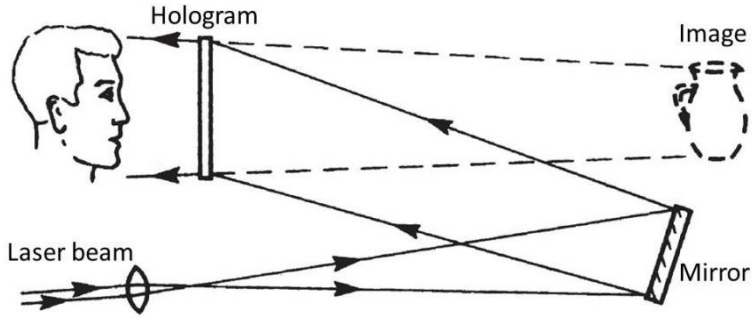

Figure 2.7 Image reconstruction

A major drawback of this technique was the poor quality of the reconstructed image, because it was degraded by the conjugate image, which was superimposed on it, as well as by scattered light from the directly transmitted beam.

The twin-image problem was finally solved when Leith and Upatnieks (16) developed the off-axis reference beam technique shown schematically in Figure 2.6 and 2.7. They used a separate reference wave incident on the photographic plate at an appreciable angle to the object wave. Therefore, when the hologram was illuminated with the original reference beam, the two images were separated by large enough angles from the directly transmitted beam, and between each other, to ensure that they did not overlap.

The development of the off-axis technique, followed by the invention of the laser, which provided a powerful source of coherent light, resulted in a surge of activity in holography that led to several important applications.

2.5.2 Optical reconstruction of a wave field

The following mathematical description makes use of the formalism introduced in the previous paragraphs. The complex amplitude of the light wave reflected by the object (object wave) is

$$E_0(x,y) = a_0(x,y)\exp(i\varphi_0(x,y)) \quad (2.33)$$

being $\boldsymbol{a_0}$ the amplitude and $\boldsymbol{\varphi_0}$ the phase. Similarly for the reference beam the complex amplitude is

$$E_R(x,y) = a_R(x,y)\exp(i\varphi_R(x,y)). \quad (2.34)$$

The intensity of the two interfering wave is

$$I = |E_0 + E_R|^2 = (E_0 + E_R)(E_0 + E_R)^* = E_R E_R{}^* + E_0 E_0{}^* + E_0 E_R{}^* + E_R E_0{}^*. \quad (2.35)$$

The intensity map recorded on the photographic plate is proportional to $I(x,y)$

$$h(x,y) = h_0 + \beta\tau I(x,y). \quad (2.36)$$

The constant β is related to the exposure efficiency of the plate, τ is the exposure time and h_0 is the amplitude transmission of the unexposed plate. $h(x,y)$ is named hologram function. In Digital Holography using CCD's as recording medium h_0 can be neglected.

For hologram reconstruction the amplitude transmission has to be multiplied with the complex amplitude of the reconstruction (reference) wave, thus reproducing analytically the physical situation descripted in Figure 2.7:

$$E_R(x,y)h(x,y) = [h_0 + \beta\tau(a_R{}^2 + a_0{}^2)]E_R(x,y) + \beta\tau a_R{}^2 E_0(x,y) + \beta\tau E_R{}^2(x,y)E_0{}^*(x,y). \quad (2.37)$$

The hologram can be regarded as a diffraction grating. The first term on the right side of this equation is the reference wave, multiplied by a factor and it represents the undiffracted wave passing the hologram (zero diffraction order). The second term is the reconstructed object

wave, forming the virtual image. The real factor $\beta\tau {a_R}^2$ only influences the brightness of the image. The third term generates a distorted real image of the object. For off-axis holography the three contribution are spatially separated.

The distortion of the real image is due to the spatially varying complex factor $E_R{}^2$, modulating the image and thus forming a conjugate object wave $E_0{}^*$. The distortion can be avoided by using the conjugate reference beam $E_0{}^*$ for reconstruction:

$$E_R{}^*(x,y)h(x,y) = [h_0 + \beta\tau({a_R}^2 + {a_0}^2)]E_R{}^*(x,y) + \beta\tau {a_R}^2 E_0{}^*(x,y) + \beta\tau {E_R}^{*2}(x,y)E_0(x,y). \quad (2.38)$$

2.5.3 The imaging equation

The position of the original object is kept in the projection of the hologram if the parameters for the reconstruction are the same of the recording process. However, if one changes the wavelength or the coordinates of the reconstruction wave source point with respect to the coordinates of the reference wave source point used in the recording process, the position of the reconstructed image changes. The coordinate shift is different for all points, thus occurring a deformation in the shape of the reconstructed object. The image magnification can depend by the reconstruction parameters, too.

The imaging equations gives a relation between the coordinates of an object point O with that of the corresponding point in the reconstructed image. An exact derivation of this equation can be found in (17).

The coordinate system is showed in Figure 2.8. Being $\mu=\lambda_1/\lambda$, the coordinates of that point in the reconstructed virtual image, corresponding to the point O are:

$$x_1 = \frac{x_P z_0 z_R + \mu x_0 z_P z_R - \mu x_R z_P z_0}{z_0 z_R + \mu z_P z_R - \mu z_P z_0}$$

$$y_1 = \frac{y_P z_0 z_R + \mu y_0 z_P z_R - \mu y_R z_P z_0}{z_0 z_R + \mu z_P z_R - \mu z_P z_0} \quad (2.39)$$

$$z_1 = \frac{z_P z_0 z_R}{z_0 z_R + \mu z_P z_R - \mu z_P z_0}.$$

The corresponding coordinates of that point in the reconstructed real image are

$$x_1 = \frac{x_P z_0 z_R - \mu x_0 z_P z_R - \mu x_R z_P z_0}{z_0 z_R - \mu z_P z_R + \mu z_P z_0}$$

$$y_1 = \frac{y_P z_0 z_R - \mu y_0 z_P z_R + \mu y_R z_P z_0}{z_0 z_R - \mu z_P z_R + \mu z_P z_0} \quad (2.40)$$

$$z_1 = \frac{z_P z_0 z_R}{z_0 z_R - \mu z_P z_R + \mu z_P z_0}.$$

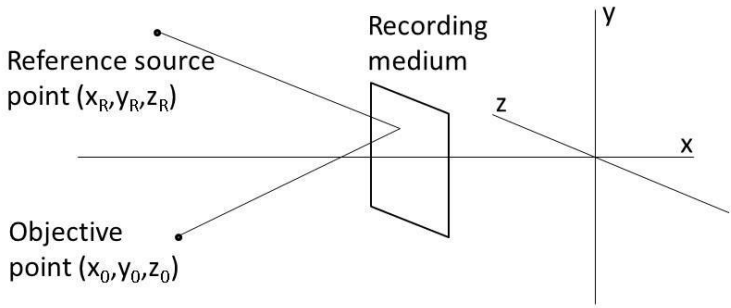

(a) Hologram recording

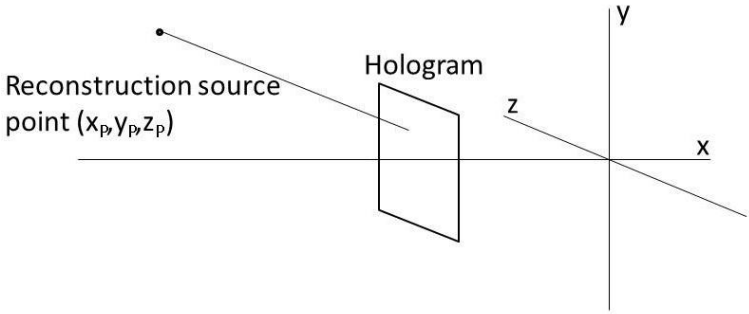

(b) Image reconstruction

Figure 2.8 Coordinate used for holographic reconstruction.

An extended object can be regarded as made up of a number of point objects. The coordinates of all surface points are described by the above-mentioned equations.

Since the real image is formed by the conjugate object wave O*, its depth is inverted. Corresponding points of the virtual image (which coincide with the original object points) and of the real image are located at equal distances from the hologram plane, but at opposite sides of it. The real image appears with the "wrong perspective". It is called a pseudoscopic image, in contrast to a normal or orthoscopic image.

2.6 Holographic interferometry

Holographic Interferometry (HI) is a method to measure optical path length variations caused by deformations of opaque reflecting bodies or refractive index variations in transparent media (18). HI is a non-contact, non-destructive method with a very high sensitivity. Optical path changes up to one hundredth of a wavelength are resolvable.

In double-exposure holography, two coherent wave fields, which are reflected in two different states of the object, interfere. The two wave fields are projected and recorded on a single photographic plate, Figure 2.9. During the first exposure the object is in its reference state, while the second exposure in recording the object in its deformed state. The hologram is then reconstructed by illumination with the reference wave, Figure 2.10. Only one image superimposed by interference fringes is visible in the recorded holograms. The observer can determine optical path changes due to the object deformation or other effects from this hologram recording.

In the real time technique the hologram is replaced, after photographical processing in the recording position. When it is illuminated with the reference wave, the reconstructed virtual image coincides with the object, thus showing the phase changes between the holographically reconstructed reference object wave and the actual object wave.

The following mathematical description is valid for the real time technique. The complex amplitude of the light wave reflected by the object (object wave) in the initial state is

$$E_1(x,y) = a(x,y)\exp(i\varphi(x,y)) \quad (2.41)$$

being $\boldsymbol{a(x,y)}$ the real amplitude and $\boldsymbol{\varphi(x,y)}$ the phase of the object wave. The shape of the object surface is described by a variation of the phase from φ to φ+Δφ, where Δφ is the difference between the reference and the actual phase. It is called interference phase. The complex amplitude of the actual object wave is therefore denoted by

$$E_1(x,y) = a(x,y)\exp[i\big(\varphi(x,y) + \Delta\varphi(x,y)\big)]. \quad (2.42)$$

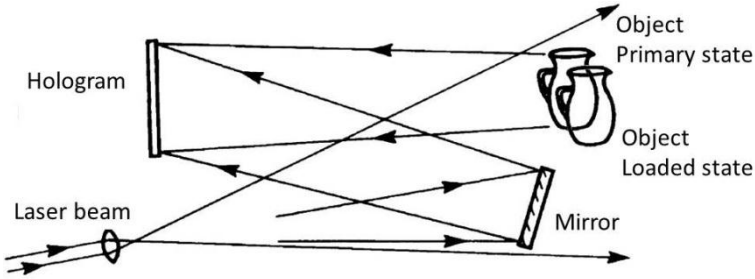

Figure 2.9 Recording of a double-exposure hologram

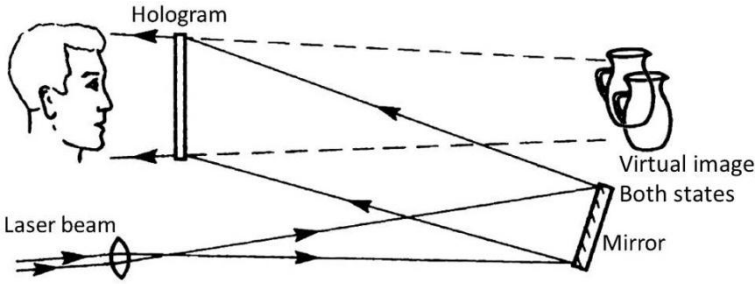

Figure 2.10 Reconstruction

The intensity of the holographic pattern is given by the square of the um of the complex amplitudes, as follows

$$I(x,y) = |E_1 + E_2|^2 = (E_1 + E_2)(E_1 + E_2)^* \quad (2.43)$$
$$= 2a^2(1 - \cos(\Delta\varphi)).$$

The relation can be rewritten as

$$I(x,y) = A(x,y) + B(x,y)\cos(\Delta\varphi). \quad (2.44)$$

The coefficients depend on the coordinates of the interferometer and cannot be known exactly because of several reasons. Let's mention for example, the non-uniform laser illumination (typically gaussian), the presence of the speckle noise, the dust contribution to the interference pattern, the non-uniform surface reflectivity etc.

Moreover, $\Delta\boldsymbol{\varphi}$ cannot be calculated directly from the measured intensity, because the parameters $A(x,y)$ and $B(x,y)$ is not known. Finally the cosine is an even function thus not defining unambiguously the sign of $\Delta\boldsymbol{\varphi}$. Therefore several techniques have been developed to determine the interference phase by recording additional information, like the Phase Shifting Interferometry described in the following paragraph.

2.6.1 Phase shifting interferometry

Phase Shifting Holographic Interferometry is a method to determine univocally the interference phase by recording additional information (19). The idea is to record three or more interference patterns with known mutual phase shifts. The equations, for a of four step phase shift, are:

$$\begin{aligned} I_1(x,y) &= A(x,y) + B(x,y)\cos(\Delta\varphi). \quad (2.45)\\ I_2(x,y) &= A(x,y) + B(x,y)\cos(\Delta\varphi + \alpha).\\ I_3(x,y) &= A(x,y) + B(x,y)\cos(\Delta\varphi + 2\alpha).\\ I_4(x,y) &= A(x,y) + B(x,y)\cos(\Delta\varphi + 3\alpha). \end{aligned}$$

In this conditions, the phase can be retrieved even without the knowledge of the shift α, as long as it is constant. The solution is:

$$\Delta\varphi = arctan\frac{\sqrt{I_1+I_2-I_3-I_4}\cdot\sqrt{3I_2-3I_3-I_1+I_4}}{I_2+I_3-I_1-I_4}. \quad (2.46)$$

2.6.2 Phase unwrapping

The exact determination of the interference phase needs a further evaluation. Being the cosine a periodic function, the interference phase distribution is indefinite to an additive integer of 2π: $\cos(\Delta\boldsymbol{\varphi})=\cos(\Delta\boldsymbol{\varphi}+2n\pi)$.

Thus interference phase maps calculated with the arctan function (or other inverse trigonometric functions) contain 2π jumps at those positions, where an extreme value of the phase (-π or π) is reached. The interference phase along a line of such a phase image looks like a saw tooth function, Figure 2.11(a). The procedure carried out to correct these jumps in order to obtain a continuous phase distribution is called phase unwrapping.

In the following one of the several phase unwrapping procedures, the so called path-dependent unwrapping algorithm, is described. A one-dimensional interference phase distribution is considered and the difference between the phase values of adjacent pixels $\Delta\boldsymbol{\varphi}(n+1) - \Delta\boldsymbol{\varphi}(n)$ is calculated. When this difference is less than -π all phase values from the n+1 pixel onwards are increased by 2π. If this difference is greater than +π, 2π is subtracted from all phase values, starting at number n+1. Otherwise the phase value remains unchanged. Practically this procedure consists in calculating first a step function, cumulating the 2π jumps Figure 2.11(b). In the last step continuous phase distribution is then calculated by adding this step function to the unwrapped phase distribution, Figure 2.11(c).

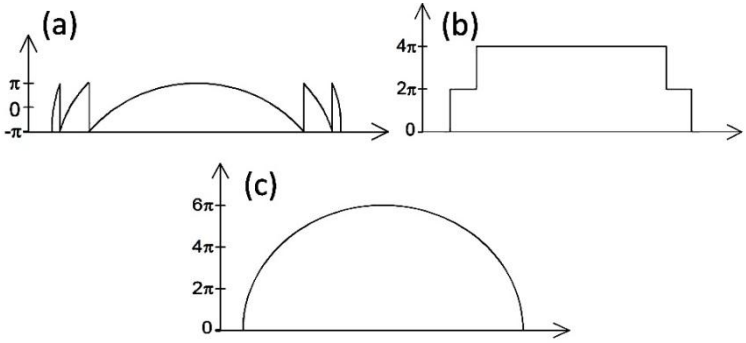

Figure 2.11 The unwrapping procedure.

Almost every pixel can be used as a starting point for this unwrapping procedure, not necessarily the pixel at the start of the line. This one-dimensional unwrapping scheme can be generalized to two dimensions. The first one row of the two dimensional phase map has to be

unwrapped with the algorithm described. Subsequently the pixels of this unwrapped row act as a starting points.

This simple unwrapping procedure described here can fail if masked regions are in the phase image due for example, to holes in the object surface. To avoid this and other difficulties several other, more sophisticated demodulation algorithm have been developed.

3. DIGITAL HOLOGRAPHY

Here an introduction to the technique called digital holography (DH) is given. The term 'digital' is referred to the recording of the hologram field, usually on a CCD or CMOS-arrays, and to the reconstruction of the wave fields that is performed numerically in a computer. Thus DH should not be confused with the computer generation of holograms then printed onto physical media, or used to drive Spatial Light Modulator, and from which the wave fields are reconstructed optically – an approach also called digital holography occasionally. In this chapter the preliminaries as well
as the main methods of numerical reconstruction are presented, forming the basis for digital holographic interferometry.

3.1 General principle

In Figure 3.1(a) the concept of digital hologram recording is showed (20). The interference pattern resulting from the superposition of a plane reference wave and the wave reflected from the object is electronically recorded on a Charged Coupled Device (CCD). The object is a three dimensional body reflecting light from its surface, whose distance from the CCD is d. The virtual image subsequent to the optical reconstruction appears at the position of the original object while the real image is formed in the opposite direction at the same distance from the CCD, see Figure 3.1(b).

The diffraction of a light wave E_R at an aperture (in this case a hologram) mounted perpendicular to the incoming beam is described by the Fresnel-Kirchhoff integral, see (2.30)

$$\boldsymbol{\Gamma(\xi',\eta') = \frac{i}{\lambda}\iint_{-\infty}^{\infty} h(x,y)E_R(x,y)\frac{e^{-i\frac{2\pi}{\lambda}\rho'}}{\rho'}\,dx\,dy} \quad (3.1)$$

where

$$\boldsymbol{\rho' = \sqrt{(x-\xi')^2 + (y-\eta')^2 + d^2}}\,. \quad (3.2)$$

$h(x,y)$ is the hologram function and ρ' the distance between a point in the hologram plane and a point in the reconstruction plane. In Figure

3.2 the geometry of the problem is shown. The inclination factor is put to 1, being the θ and θ' angles both close to zero. A reference plane wave will be considered

$$E_R = a_R + i0 = a_R \quad (3.3)$$

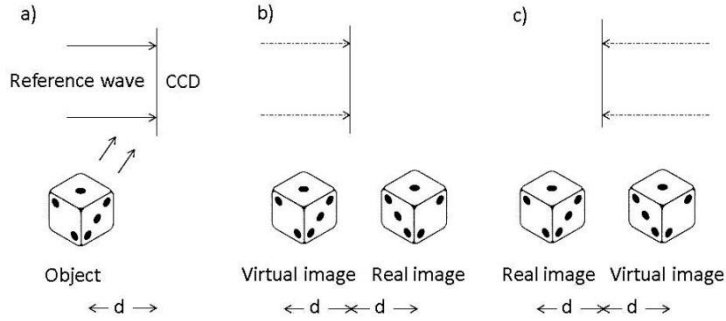

Figure 3.1 Digital holography a) recording b) reconstruction with E_R b) reconstruction with E_R^*

The complex field is reconstructed at a distance d behind the CCD plane, that means in the plane of the real image. From the complex reconstructed field, moreover, both the phase and the intensity information can be deduced, unlike the optical holography were only the intensity in made visible.

In (2.37) it is shown that the conjugate reference beam to reconstruct an undistorted real image can be produces. Thus to achieve an undistorted real image in Digital Holography it is therefore necessary to insert E_R^* instead of E_R in Eq. (3.1):

$$\boldsymbol{\Gamma(\xi,\eta) = \frac{i}{\lambda}\iint_{-\infty}^{\infty} h(x,y) E_R^*(x,y) \frac{e^{-i\frac{2\pi}{\lambda}\rho}}{\rho} dx\, dy} \quad (3.4)$$

where:

$$\rho = \sqrt{(x-\xi)^2 + (y-\eta)^2 + d^2}\,. \quad (3.5)$$

The above depicted experimental situation is shown in Figure 3.1(c). The real image emerges where the object was located during recording.

In case of a plane reference wave defined in (3.3) both reconstruction formulas, Eq. (3.1) and (3.4), are equivalent because $E_R = E_R^*$.

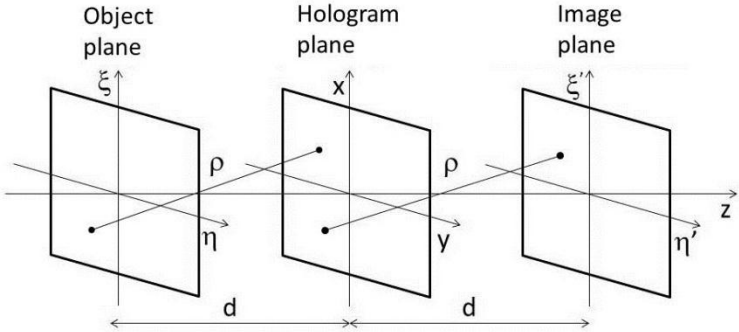

Figure 3.2 The reconstruction scheme.

The set-up of Figure 3.1 with a plane reference wave impinging perpendicularly onto the CCD is often used in Digital Holography.

3.2 Numerical reconstruction

Once the hologram is recorded on the CCD, it is necessary to obtain a numerical algorithm, deduced by (3.4), to process the acquired information and retrieve the whole optical field. Different approaches have been developed, we present in the following a review of the most common solutions.

3.2.1 Reconstruction via the Fresnel approach

For x and y values as well as for ξ and η values which are small compared to the distance d between the reconstruction plane and the CCD expression can be replaced by the first terms of the Taylor series:

$$\rho = d + \frac{(\xi - x)^2}{2d} + \frac{(\eta - y)^2}{2d} - \frac{1}{8}\frac{[(\xi - x)^2 + (\eta - y)^2]}{d^3} + \cdots \approx$$

$$d + \frac{(\xi - x)^2}{2d} + \frac{(\eta - y)^2}{2d}. \qquad (3.6)$$

Replacing in (3.4) the denominator by the above relations we obtain

$$\Gamma(\xi,\eta) = \frac{i}{\lambda d} exp\left(-i\frac{2\pi}{\lambda}d\right) \iint_{-\infty}^{\infty} h(x,y)E_R(x,y)$$

$$exp\left[-i\frac{\pi}{\lambda d}((\xi - x)^2 - (\eta - y)^2)\right] dx\, dy \quad (3.7)$$

that becomes, carrying out the factors not to be integrated

$$\Gamma(\xi,\eta) = \frac{i}{\lambda d} exp\left(-i\frac{2\pi}{\lambda}d\right) exp\left[-i\frac{\pi}{\lambda d}(\xi^2 - \eta^2)\right]$$
$$\iint_{-\infty}^{\infty} h(x,y)E_R(x,y)\ exp\left[-i\frac{\pi}{\lambda d}(x^2 - y^2)\right] \times$$
$$exp\left[-i\frac{\pi}{\lambda d}(x\xi - y\eta)\right] dxdy\,. \quad (3.8)$$

This equation is called *Fresnel transformation*. It allows to reconstruct the wavefield in a plane behind the hologram, in this case in the plane of the real image. The intensity and the phase are calculated as follows

$$I(\xi,\eta) = |\Gamma(\xi,\eta)|^2 \quad \varphi(\xi,\eta) = arctan\frac{Im(\Gamma(\xi,\eta))}{Re(\Gamma(\xi,\eta))} \quad (3.9)$$

where *Re* and *Im* denote, respectively, the real and imaginary part. We can now take into account the discrete nature of the acquired hologram. By introducing the following substitutions (21)

$$\nu = \frac{\xi}{\lambda d}; \quad \mu = \frac{\eta}{\lambda d}. \quad (3.10)$$

The (3.8) becomes

$$\Gamma(\nu,\mu) = \frac{i}{\lambda d} exp[-i\pi\lambda d(\nu^2 + \mu^2)] \iint_{-\infty}^{\infty} h(x,y)E_R(x,y)$$
$$exp\left[-i\frac{\pi}{\lambda d}(x^2 - y^2)\right]\ exp[-i\pi\lambda d(x\nu + y\mu)]dxdy\,. \quad (3.11)$$

by omitting the constant phase factor exp(-i2π/λd).

By comparing the equation (3.11) with the definition of the two-dimensional Fourier transform we can rewrite it as the inverse Fourier transformation of $h(x,y)\mathrm{E_R}(x,y)\exp(-i2\pi/\lambda d(x^2+y^2))$

$$\Gamma(\nu,\mu) = \frac{i}{\lambda d} exp[-i\pi\lambda d(\nu^2+\mu^2)]$$
$$\times \mathfrak{F}^{-1}\left\{E_R(x,y)h(x,y)exp\left[-i\frac{\pi}{\lambda d}(x^2+y^2)\right]\right\}. \quad (3.12)$$

If the hologram function is acquired on a rectangular grid of a N × N points, with step of Δx and Δy the function Γ can be digitized. Δx and Δy are the distances between the neighboring pixels on the CCD in the two directions. Discretizing the integral in (3.12) we obtain

$$\Gamma(m,n) = \frac{i}{\lambda d} exp[-i\pi\lambda d(m^2\Delta\nu^2 + n^2\Delta\mu^2)]$$
$$\times \sum_{k=0}^{N-1}\sum_{l=0}^{N-1} E_R(k,l)h(k,l)exp\left[-i\frac{\pi}{\lambda d}(k^2\Delta x^2 + l^2\Delta y^2)\right]$$
$$\times exp[i2\pi(k\Delta x m\Delta\nu + l\Delta y n\Delta\mu)]. \quad (3.13)$$

In accordance with the theory of the Fourier transform (22) the following relation are valid

$$\Delta\nu = \frac{1}{N\Delta x} \quad \Delta\mu = \frac{1}{N\Delta y}. \quad (3.14)$$

The relations between the spatial variables in the image and hologram plane are

$$\Delta\xi = \frac{\lambda d}{N\Delta x} \quad \Delta\eta = \frac{\lambda d}{N\Delta y}. \quad (3.15)$$

By substituting the variables in the equation (3.13) we obtain the Fresnel discrete transform

$$\Gamma(m,n) = \frac{i}{\lambda d} exp\left[-i\pi\lambda d\left(\frac{m^2}{N^2\Delta x^2} + \frac{n^2}{N^2\Delta y^2}\right)\right]$$
$$\times \sum_{k=0}^{N-1}\sum_{l=0}^{N-1} E_R(k,l)h(k,l)exp\left[-i\frac{\pi}{\lambda d}(k^2\Delta x^2 + l^2\Delta y^2)\right]$$
$$\times exp\left[i2\pi\left(\frac{km}{N} + \frac{ln}{N}\right)\right]. \quad (3.16)$$

This is the discrete Fresnel transform. The matrix Γ is calculated by multiplying $E_R(k, l)$ with $h(k, l)$ and $\exp[-i\pi/(\lambda d)(k^2\Delta x^2 + l^2\Delta y^2)]$ and applying an inverse discrete Fourier transform to the product. The calculation is done most effectively using the fast Fourier transform

(FFT) algorithm. The factor in front of the sum is only affecting the phase and can be neglected for most applications.

In accordance to (3.15) the pixel distances in the reconstructed image, Δξ and Δη, are different from those of the hologram matrix. At first sight it looks like a change of resolution by applying the numerical Fresnel transform. Actually the (3.15) is connected to the diffraction-limited resolution of optical systems: the hologram is the aperture of the optical system with side length NΔx. According to the theory of diffraction at a distance d behind the hologram a diffraction pattern develops. $\Delta\xi = \lambda d/N\Delta x$ is thus the diameter of the Airy disk in the plane of the reconstructed image, and it constitutes a limit to the resolution of the image reconstructed by a discrete Fresnel transform.

3.2.2 Reconstruction by the convolutional approach

Since the direct numerical processing of the Fresnel–Kirchhoff integral (3.1) is time consuming, an equivalent formulation for numerical processing has been developed. This formulation is based on the convolution theorem and is called the 'convolution approach'. The mathematics is well known since the early days of holography. Demetrakopoulos and Mittra (23) first applied this way of processing for numerical reconstruction of suboptical holograms. Later this approach was applied to optical holography. The diffraction formula (3.1) is thus a superposition integral:

$$\Gamma(\xi,\eta) = \iint_{-\infty}^{\infty} h(x,y)E_R(x,y)g(\xi,\eta,x,y)\ dx\ dy \quad (3.17)$$

where the impulse function is given by

$$g(\xi,\eta,x,y) = \frac{i}{\lambda d}\frac{exp\left[-i\frac{2\pi}{\lambda}\sqrt{(x-\xi)^2+(y-\eta)^2+d^2}\right]}{\sqrt{(x-\xi)^2+(y-\eta)^2+d^2}}. \quad (3.18)$$

The linear system characterized by $g(\xi, \eta, x, y) = g(\xi - x, \eta - y)$ is space-invariant: the superposition integral is a convolution. The convolution theorem, which states that the Fourier transform of the convolution of $h \cdot E_R$ with g is the product of the individual transforms $\mathfrak{F}\{h \cdot E_R\}$ and $\mathfrak{F}\{g\}$. $\Gamma(\xi, \eta)$ can be calculated by multipling the Fourier transform of $h \cdot E_R$ with the Fourier transform of g, and taking an inverse Fourier transform of this product. All three Fourier transforms are needed, carried out using the FFT algorithm.

The discretization of the impulse function is given by

$$g(k,l) = \frac{i}{\lambda}\frac{exp\left[-i\frac{2\pi}{\lambda}\sqrt{(k-\frac{N}{2})^2\Delta x^2+(l-\frac{N}{2})^2\Delta x^2+d^2}\right]}{\sqrt{(k-\frac{N}{2})^2\Delta x^2+(l-\frac{N}{2})^2\Delta x^2+d^2}}. \quad (3.19)$$

The relation for retrieving Γ is given by

$$\mathfrak{F}\{\Gamma(\xi,\eta)\} = \mathfrak{F}\{\mathrm{h}\cdot \mathrm{E}_R\}\mathfrak{F}\{g\}. \quad (3.20)$$

By calculating the Fourier transform of g we obtain

$$G(n,m) = exp\left[-i\frac{2\pi d}{\lambda}\sqrt{1-\frac{\lambda^2\left(n+\frac{N^2\Delta x^2}{2d\lambda}\right)}{N^2\Delta x^2}-\frac{\lambda^2\left(m+\frac{N^2\Delta y^2}{2d\lambda}\right)}{N^2\Delta y^2}}\right] \quad (3.21)$$

We can thus retrieve the value of Γ by solving two Fourier transforms

$$\mathfrak{F}\{\Gamma(\xi,\eta)\} = \mathfrak{F}^{-1}\{\mathfrak{F}\{\mathrm{h}\cdot \mathrm{E}_R\}\cdot \mathrm{G}\}. \quad (3.22)$$

The pixel sizes of the images reconstructed by the convolution approach are equal to that of the hologram, being thus different from those of the Fresnel approximation. In any case the image resolution does not change due to the physical limits already discussed at the end of the previous section. The convolution approach is advantageously applied to reconstruct in-line holograms from particle distributions within transparent media.

3.2.3 Fourier Holography

In Figure 3.3 is the optical configuration known as lensless Fourier holography is depicted. It has been also realized in Digital Holography (24). The source of the spherical reference wave and the object are located in the same plane. The reference wave at the acquisition plane is given by

$$E_R = \frac{exp\left(-i\frac{2\pi}{\lambda}\sqrt{(d^2+x^2+y^2)}\right)}{\sqrt{(d^2+x^2+y^2)}}$$
$$\approx \frac{1}{d}\exp\left(i\frac{2\pi}{\lambda}\right)\exp\left(i\frac{\pi}{\lambda d}(x^2+y^2)\right) \quad (3.23)$$

Inserting the retrieved E_R in the reconstruction formula for the virtual image, the following equation is obtained

$$\Gamma(m,n) = Cexp\left[\frac{i}{\lambda d}(\xi^2+\eta^2)\right]\Im^{-1}\{h(x,y)\} \quad (3.24)$$

being C a complex constant. A lensless Fourier hologram is therefore reconstructed by a Fourier transform. However reconstruction at different distances cannot be retrieved. The spherical phase factor multiplying the Fourier transform can be eliminated using a spherical reference wave with the same curvature.

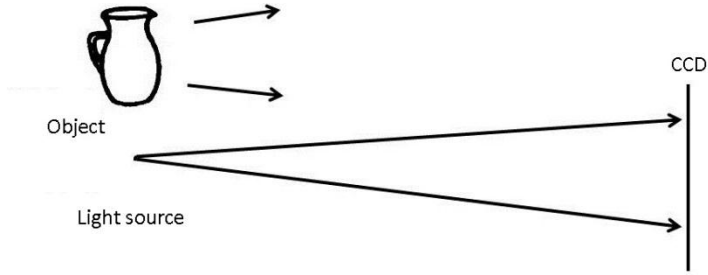

Figure 3.3 Setup for Fourier Holography.

3.2.4 Suppression of the DC term

The bright square in the centre of Figure 3.4(a) is the undiffracted reconstruction wave. This zero order or DC term disturbs the image, covering the objects parts lying behind. Several methods have been developed to suppress this term (25). To understand the cause of this DC term hologram formation according Eq. (2.34) is considered. The equation is rewritten by inserting the definitions of E_R, E_0 and multiplying the terms:

$$I = {E_r}^2 + {E_0}^2 + 2E_R E_0 \cos(\varphi_0 - \varphi_R). \quad (3.25)$$

The first two terms are representing the DC term in the reconstruction process. The value of the third term is statistically varying between $\pm 2aE_RE_0$ from pixel to pixel at the CCD. The average intensity of all pixels of the hologram matrix is

$$I_m = \frac{1}{N^2}\sum_{k=0}^{N-}\sum_{l=0}^{N-1} I(k\Delta x, l\Delta y) \quad (3.26)$$

The DC term can be eliminated by subtracting I_m from the hologram

$$I' = I(k\Delta x, k\Delta y) - I_m(k\Delta x, k\Delta y) \quad (3.27)$$

for k, l=0,…,N-1.

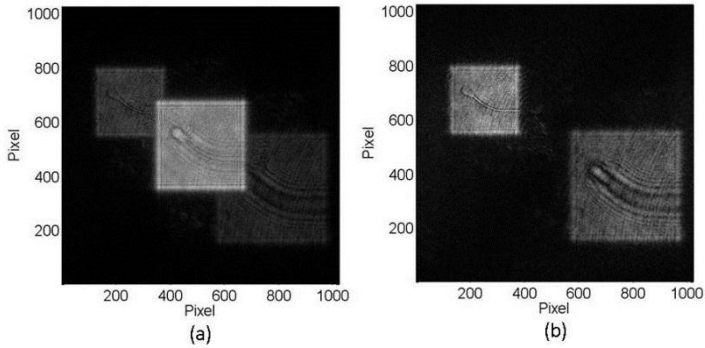

Figure 3.4 Before (a) and after (b) the suppression of the DC term.

It is also possible to filter the hologram matrix by a high-pass with low cut-off frequency. Another method to suppress the DC term is to measure the intensities of reference wave E_R^2 and object wave E_O^2 separately. Afterwards an image free from the DC term can be calculated by subtracting the intensities from the hologram before reconstruction. However, this procedure has the disadvantage to require higher experimental effort due to the additional measurements.

3.2.5 Fourier optics described by operator algebra

An interesting approach for the analysis of the propagation problem by means of the operator algebra has been proposed by J. Sahimir (26). Fresnel diffraction is described by replacing the Fresnel-Kirchhoff integral, the lens transfer factor, and other operations by operators. The resulting operator algebra leads to the description of Fourier optics in a simple and compact way, bypassing the cumbersome integral calculus. The detail of the formalism can be found in (26). By means of this

approach the propagated field $u_o(\xi,\eta)$ in function of the initial field $u_i(x,y)$ (3.4) can be rewritten as

$$u_o(\xi,\eta) = exp(ikd)\left\{\mathfrak{F}^{-1}\left[exp\left(-\frac{ikd\lambda^2}{2}(\upsilon^2+\mu^2)\right)\right][\mathfrak{F}(u_i(u,y))]\right\} \quad (3.28)$$

being ν and μ are the spatial frequencies already defined in (3.10) For digital reconstruction (3.28) is implemented in a discrete form (27)

$$\Gamma(m,n) = exp(ikd)\left\{\mathfrak{F}_D{}^{-1}\left[exp\left(-\frac{ikd\lambda^2}{2N^2d^2}(U^2+V^2)\right)\right][\mathfrak{F}_D u_i(h,k)]\right\} \quad (3.29)$$

where N is the number of pixels in both directions, m, n, U, V, h and k are integer numbers varying from 0 to N-1. The discretized Fourier transform is defined as

$$\mathfrak{F}_D\{g(k,l)\} = \frac{1}{N}\sum_{k,l=0}^{N-1} exp\left[-\frac{2\pi i}{N}(mk+nl)\right] g(k,l). \quad (3.30)$$

3.3 Recording of digital holograms

As pointed out in the introduction, the hologram is recorded on a digital device. In the following the main characteristics of the recording digital device and the relative technical requirement will be described.

3.3.1 Charged-coupled Devices

A Charged-Coupled Devices (CCD's) is an electrical device used to create images of objects, store information or transfer electrical charge. The main application today is image recording. CCD's are used as imaging devices in electronic cameras (video and still imaging) and scanners. They are available as line scanning devices or as rectangular matrix of light detectors. For DH the latter architecture is of interest. The mechanism of light recording is the following. The incident light separates charges by the internal photo effect and is thus converted into an electronic charge at the individual detectors called pixels. The charge transfer function moves the packets of charge within the semiconductor (silicon) substrate to memory cells. The capacitor matrix of the memory cells converts the transferred charge to a voltage and an amplifier adapts the voltage to the output requirements. The three basic architectures of CCD's are called interline transfer devices, frame transfer devices and full- frame-transfer devices.

Interline transfer devices (Figure 3.5(a)) consist of a striped pattern of light sensitive detectors (photodiodes) and of separated non-sensitive or light shielded storage devices. The charge packages generated in the light sensitive pixels are shifted into the adjacent storage devices by a parallel clock. The charges in these storage devices are then shifted line by line into the serial register. This serial register transfers the charge packages into a charge to voltage converter with amplifier thus forming the output signal. The major disadvantage of interline transfer CCD's is their complexity, since it is necessary to separate the photodetecting and storage (readout) functions.

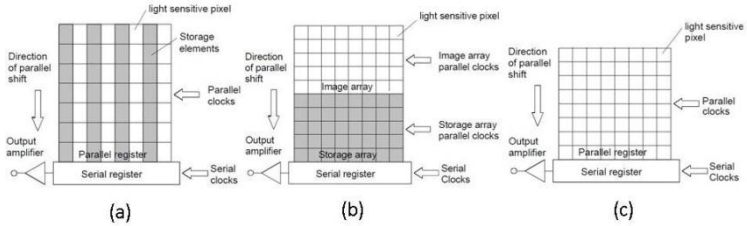

Figure 3.5 Interline-transfer architecture (a); Frame-transfer architecture (b); Full-transfer architecture (c).

Frame-transfer CCD's also have different areas for light conversion and for storage. These elements are divided into two different blocks (Figure 3.5(b)). The idea is to shift a captured scene from the photosensitive image array very fast to the storage array. The readout from the storage register is performed similar to the readout process of interline transfer devices.

Full-Frame CCD's have the simplest architecture (Figure 3.5(b)). They don't have a separated storage area and the entire sensor area is light sensitive. The photons of the illuminating light are converted into charge packages. The resulting rows of image information are then shifted in parallel to the serial register that subsequently shifts the row of information to the output as a serial stream of data. The process repeats until all rows are transferred off chip. Since the parallel register is used for both image detection and readout, a mechanical shutter is needed to preserve scene integrity. Full-frame CCD's have highest resolution and the production costs are comparably cheap.

In principle all three types of CCD's are suitable for Digital Holography. For full frame type CCD's the exposure time can be adjusted according to the demands of a specific application. Even exposure times in the range of seconds are possible, even if the mechanical shutter limits the number of holograms, which can be recorded per second (frame rate). In addition the shutter may cause mechanical vibrations to the set-up, reducing the hologram quality. An advantage of interline transfer type CCD's is that such devices are equipped with an electronic shutter, allowing higher frame rates. The best camera choice is dependent in general on the specific holographic application.

3.3.2 Spatial frequency requirement

One of the main request for DH application of a camera is to resolve the frequency of the interference pattern created by the superposition wave with the one scattered by the object. The maximum spatial frequency to be resolved is given by the angle $\theta_{\max}$ between the waves

$$f_{max} = \frac{2}{\lambda} sin\left(\frac{\theta_{max}}{2}\right). \quad (3.31)$$

The resolution for photographic emulsion is about 5000 lines for mm, thus allowing the recording of holograms with angles higher than 180° between the reference and the object wave. However, the distance between two neighboring pixels is only about 5μm. The achieving resolution is thus limited to 100 lines for mm.

3.4 Digital holographic microscopy

A typical setup for digital holographic microscopy is shown in Figure 3.6. The light diffused (a) or transmitted (b) by the sample S, after the magnification by the microscope objective MO, interferes with the reference wave. The resulting hologram is then recorded by the CCD camera.

The main problem in retrieving of the quantitative phase map of the resulting hologram is due to the presence on the optical path of strongly focusing optics i.e. the microscope objective. In fact these optics introduce in the transmitted field a parabolic phase factor, whose presence hides the phase information due to the sample under study.

Denoting with ϕ_0 the phase scattered or reflected by the object, we can write the phase ϕ reconstructed for the single digital hologram as

$$\phi(x,y) = \phi_0(x,y) + \frac{ik}{2R}(x^2 + y^2) \quad (3.32)$$

where the quadratic term that is due to the defocus aberration coming from the curvature R introduced by the microscope objective used to image the sample. Such a term hinders the possibility of obtaining $\phi_0(x,y)$. To recover quantitative phase in DH, it is than necessary to remove the parabolic phase factor, showed in Figure 3.7, from the reconstructed phase map, and various strategies can be adopted for retrieving the correct phase map.

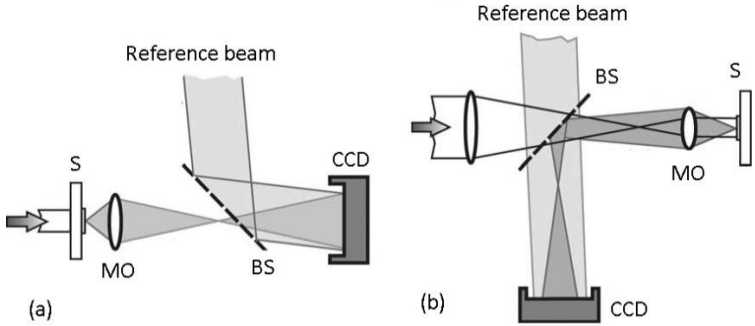

Figure 3.6 Digital Holographic Microscopy setup, in transmission (a) and in reflection (b).

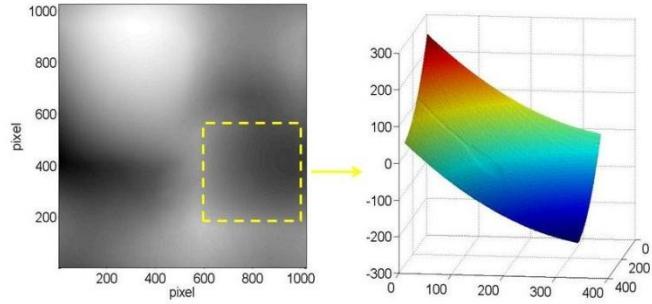

Figure 3.7 Parabolic phase factor in the reconstructed phase map.

However, from the conceptual point of view, the parabolic or defocus phase factor is removed by subtracting the phase map obtained from a synthetic or a real digital hologram. In one of the methods proposed by Ferraro et al. (28) the correcting phase mask is obtained by the acquisition of a second digital hologram. The first exposure is made of the object under investigation, whereas the second one is made of a flat reference surface in proximity of the object. This second hologram contains information about all the aberrations introduced by the optical components including the defocusing due to the microscope objective. By manipulating the two holograms numerically, it is possible to compensate for these aberrations. The phase distribution in the image plane is given by

$$\phi(n,m) = arg\left[\frac{b_0{}'(m,n)}{b_R{}'(m,n)}\right] \quad (3.33)$$

where $b'_0(n,m)$ and $b'_R(n,m)$ are the complex wavefields calculated at distance d' from the object hologram and the reference hologram, respectively. The requirement for a flat surface is well satisfied when MEMS structures are inspected, because the micro-machined parts are typically fabricated on a flat silicon substrate. In that case the area around the structure offers a good plane surface that can be used as reference. This technique allows to compensate all the undesired phase factors introduced by the optical elements in the setup; so double-exposure appears the best way to recover quantitative phase information on sample object. Anyway it has some drawbacks such as it's not applicable in case of samples lacking of flat surrounding surface, i.e. biological sample where an high cells density doesn't permit the selection of a plane area. Moreover, double acquisition and double computation increase the calculation time. A numerical technique has been developed in 2006 (29): combining the concept of lateral shear interferometry (LSI) within a digital holography microscope, it is possible to obtain quantitative optical phase measurement in microscopy by a new single image-processing procedure. To determine $\phi_0(x,y)$ in (3.33) we simply introduce digitally, in the reconstructed image plane, two lateral shears, $\Delta\phi_x$ and $\Delta\phi_y$, in the x and y directions, respectively, of the wavefront of (3.32), namely, $\Delta\phi_x = \phi(x,y) - \phi(x-s_x,,y)$ and $\Delta\phi_y = \phi(x,y) - \phi(x,,y-s_y)$. The two maps $\Delta\phi_x$ and $\Delta\phi_y$ are related to the

first-order derivative of the wave front if the amount of the shear s_x and s_y is small. In fact, according to the finite- finite-difference approximation approach we have

$$\frac{\partial\phi(x,y)}{\partial x} \approx \frac{\Delta\phi_x}{s_x} \qquad \frac{\partial\phi(x,y)}{\partial y} \approx \frac{\Delta\phi_y}{s_y}. \quad (3.34)$$

The latter equations can be written in terms of the finite-difference approximation of object phase distribution $\phi_0(x,y)$ in the following form

$$\frac{\partial\phi(x,y)}{\partial x} \approx \frac{\phi_0(x,y)-\phi_0(x-s_x,y)}{s_x} + \frac{iks_x x}{R}$$

$$\frac{\partial\phi(x,y)}{\partial y} \approx \frac{\phi_0(x,y)-\phi_0(x,y-s_y)}{s_y} + \frac{iks_y y}{R}. \quad (3.35)$$

The subtraction of the linear term, representing the contribution made by the defocus aberration, from the digital shearograms gives the digital shearograms $\Delta\phi_{0,x}= \phi_0(x,y)-\phi_0(x-s_x,y)$ and $\Delta\phi_{0,y}= \phi(x,y)-\phi(x,y-s_y)$. From the knowledge of the differences $\Delta\phi_{0,x}$ and $\Delta\phi_{0,y}$ along the x and y directions, object phase distribution $\phi_0(x+\Delta x, y+\Delta y)$ at mesh point $(x+\Delta x, y+\Delta y)$ can be determined from its finite difference approximation, i.e.,

$$\phi_0(x+\Delta x, y+\Delta y) \approx \phi_0(x,y) + \Delta\phi_0(x,y)\Delta x + \Delta\phi_0(x,y)\Delta y \quad (3.36)$$

by standard integration numerical procedures. The above-depicted procedure is limited by the numerical routines for standard integration, usually needing a flat and spikeless background. This limitation will be overcome in the following chapters.

It is useful to introduce the concept of Optical Phase Difference (OPD) for the following application to cell analysis by DHM in transmission

$$OPD = \frac{\lambda}{2\pi}\phi(m,n) = s(m,n)(n_c - n_S) \quad (3.37)$$

where $s(m,n)$ is the thickness of the cell and n_c and n_s are the refractive index of the cell and the surrounding medium respectively.

3.4.1 Self-focusing criterion in DHM

As described in the previous paragraphs, DHM provides a numerical investigation of the third dimension by performing a plane-by-plane refocusing. However, it does not provide any criterion when the best focus distance is reached. Indeed, if digital holographic reconstruction can refocus a sample slice-by-slice as the focusing stage of a classical imaging system, the refocusing degree of an object has to be determined by an external criterion. Several different solutions have been developed, the one we describe here, proposed by F. Dubois (30), is based on an amplitude analysis. Biological cells are mostly transparent and can be considered as pure phase objects. It is assumed that a pure phase object is illuminated in transmission by a plane wave that is propagating along the z axis and that the physical thickness of the object is small in comparison with the depth of focus of the imaging system. Moreover, it is assumed that the object is located at a distance d with respect to the focus plane of the imaging system. The beam emerging out of the object is expressed by

$$u_d = a\, exp[i\phi(x,y)] \quad (3.38)$$

where ϕ(x,y) is the optical phase change introduced by the phase object and a is the uniform real amplitude of an illuminating plane wave. As we consider a pure phase object, the emerging intensity is constant when the focus image of the object is reached. Indeed the intensity image of the object disappears from the focus image as it is well known in optical microscopy. It results also that the modulus of the amplitude is constant in the focus plane. When the image of the object is defocused, the refraction created by the object's phase modulates the amplitude and the resulting intensity. As a consequence the defocus is at the origin of fluctuations of the amplitude modulus and the intensity. The refocus distance d is fulfilling the condition $\iint_{-\infty}^{\infty}|u_d(x,y)|$=constant. Switching to the discrete case, the optical field emerging from the object can be written as

$$u_s = a\, exp\left[i\phi_s\right] \quad (3.39)$$

being s=1,…,N the sampling parameter. It can be demonstrated (30) that the self-focusing criterion is connected to the parameter

$$M_d = \sum_{s=0}^{N-1} a_s \quad (3.40)$$

In particular M_d is maximum when the best focus plane is reached.

4. DEVELOPMENT OF THE EXPERIMENT

The first part of the research activity reported in this work has been devoted to the development of the experiment. For data acquisition manly two different optical setups have been used: a classical Digital Holographic Microscope (DHM), working with a fully coherent source has been mounted and optimized, and a DHM working in partially coherent regime, developed by Prof. F. Dubois (31) has been used during a 7 months internship at the Microgravity Research Centre of the Univerité Libre de Bruxelles. Moreover, a technological procedure for the achievement of microfluidic structures has been carried out.

4.1 The optical setup

Even if the interferometric setup for DHM is on the whole quite simple, a big attention has been dedicated to the optimization of the characteristic of the acquired holograms, such as fringe pattern contrast and frequency, background flatness, etc. A general DHM Mach-Zehnder interferometer will be described followed by a description of the important improvements achieved by the use of a partial coherent source.

4.1.1 The Mach-Zehnder interferometer

The employed experimental setup for DHM working in fully coherence is shown in Figure 4.1. The laser light from an He-Ne (whose wavelength is 633 nm), splitted by the first beam splitter in two arms, is expanded and filtered. One of the two beam, named the object beam, after passing through the sample S, is magnified and mixed with the reference beam. The phase $\phi(x, y)$ incorporates information about the topographic profile of the object under investigation because it is related to the optical path difference (OPD) that depends on the refractive index and thickness both of the sample under study and the material containing the object itself. Since all light-sensitive sensors respond to intensity only, the phase is encoded in the intensity fringe pattern. The hologram is proportional to the intensity of this interference pattern. In our setup, the hologram is acquired by a charge

coupled devices (CCD) camera array i.e., a 2-D rectangular raster of 1024 × 1392 pixels, with pixel pitches Δx=4.7 μm in the two directions. A λ/2 wave-plate is present on the objet arm and the axis-angle is chosen in order to increase the fringe contrast.

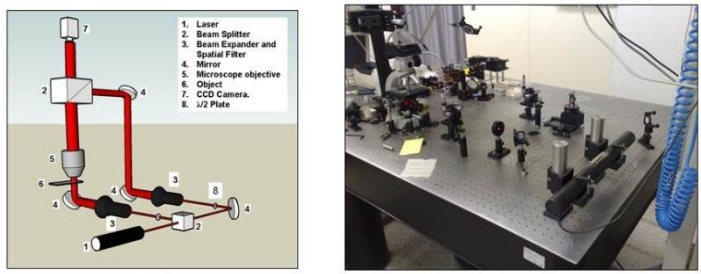

Figure 4.1 Sketch (a) and picture (b) of the experimental setup.

4.1.2 DHM working with a partial spatially coherent source

The optical for DHM working with a laser is schematized in Figure 4.2 (27) (32). The coherent source, (a mono-mode laser diode, λ=635nm) is transformed into a partially spatial coherent source by focusing the beam, by lens L1, close to the plane, with a rotating ground glass (RGG). It has been demonstrated that a coherent beam incident on a moving ground glass behaves like a spatially partial coherent source, provided that the ground-glass motion is statistically averaging the optical properties of the outgoing laser beam (33). The partial spatial coherence is adjusted by changing the position of the focused spot with respect to the RGG plane. The Lens L2 (focal length f_2=50mm) collimates the beam that is divided by a beam-splitter BS1. As in the previous case, the object beam illuminates the sample S by transmission. When the RGG is stopped the speckle size can be measured in the object plane to control the spatial coherence. A plane of the sample is imaged by the couple of lenses L3-L5 on the CCD camera sensor, interfering with the reference beam. An optical flat, not indicated in Figure 4.2, is placed in front of the lens L4 to equalize the optical path of the reference and object beam. The camera is a JAI CV-M4 with a CCD array of 1280×1024 pixels (subsequently cropped to

1024×1024 to match the Fast Fourier Transform computation). The camera exposure time is 100 μs.

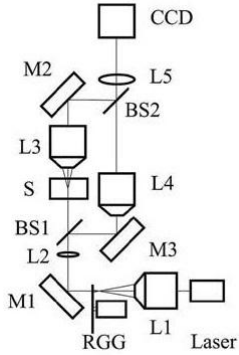

Figure 4.2 DHM working with a partially spatial coherent source from a laser beam (31).

The complex field of the object beam is reconstructed numerically from the frequency spectrum of the acquired hologram. The off-axis configuration of the employed set-up allows a spatial separation of the diffraction orders due to the holographic reconstruction. Thus, the first diffraction order can be separated from the whole spatial frequency spectrum with a bandwidth filter and shifted to the origin of the plane, thus obtaining the spectrum of $\Gamma(x,y)$, except for a constant (34).

Partial coherent illumination also removes the multiple reflections that can occur with coherent illumination. In fact we assume that a reflection introduces an increase of the optical path *d*. If the distance *d* introduces a significant decorrelation of the speckle pattern, the contrast of the interference fringe pattern between the reflected beam and the direct beam is reduced.

A major issue of the full coherent illumination if the coherent speckle noise that arises on the unavoidable defects of the optical system, on the sample containers that can be in some cases of poor optical quality and on the sample itself when it is bulky and scatters the light. The speckle results from the coherent superposition of random contributions that originate from out of focus locations. A way to reduce the strength of the speckle noise is to reduce the spatial coherence of the beam

illuminating the sample. An example from a fluid physics experiment is shown: the images of Figure 4.3 (32)are magnified parts of digital holograms that were recorded with a fully coherent illumination and a partially spatial illumination. The object is identical and consists of 5μm particles immerged in distilled water. In the partially spatial coherent case (b), the diffraction pattern of the unfocused particles is clearly distinguishable and the digital holographic reconstruction can be applied to refocus the particles in the field of view. On the contrary, with the full coherent illumination (a), the only visible particles are those that are focused and the background thus producing a very noisy digital holographic refocusing is very noisy.

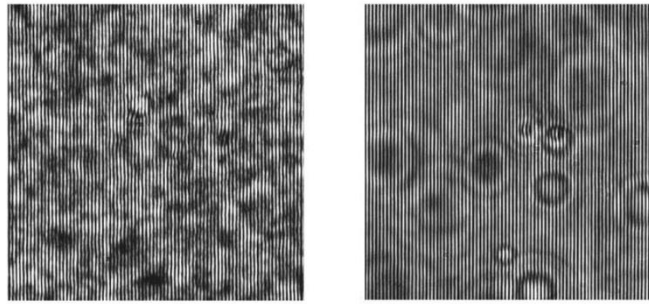

Figure 4.3 Interferometric image of particles in distilled water with fully (a) and partial spatially coherent (b) illumination (courtesy of Prof. F. Dubois (32))

4.2 Fabrication of the microfluidic chip

In order to evaluate the characteristic of the biological sample in their native environment and to develop an integrated setup for sorting compatible with DHM a microfluidic device should be developed. The use of Polydimethylsiloxane (PDMS) elastomer for miniaturized bioassays has numerous advantages over silicon and glass. PDMS as a material is inexpensive, flexible, and optically transparent down to 230 nm (and therefore compatible with many optical methods for detection). It is compatible with biological studies because it is impermeable to water, nontoxic to cells, and permeable to gases. A final, major advantage of PDMS over glass and silicon is the ease with which it

can be fabricated and bonded to other surfaces. For the development of bioassays, where many designs may need to be tested, the ease of rapid prototyping in PDMS is a critical advantage. Procedures for the fabrication of PDMS structures for microfluidics have been described in detail elsewhere (35). Briefly, the design of the microstructures is made in a computer-aided design (CAD) program. Using commercial services, the CAD-generated patterns are printed on transparencies. The transparency is then used as a photomask in UV-photolithography to generate a master. In this procedure, a thin layer of photoresist (for example, the photocurable epoxy SU-8) is spin-coated onto a silicon wafer. Using different types of SU-8 of various viscosities, thicknesses of 1–300 mm can be reliably spin-coated. The photoresist is exposed to UV light through the photomask, and a developing reagent is used to dissolve the unexposed regions. The resulting bas-relief structure serves as a master for fabricating PDMS molds. To create the PDMS mold, the surface of the silicon/photoresist master is treated with fluorinated silanes (which prevents irreversible bonding to PDMS), and a liquid PDMS prepolymer (in a mixture of 1:10 base polymer:curing agent) is poured onto it. The PDMS is cured at 707C for 1 h or more and peeled off the master, producing the final replica bearing the designed microstructures. Small holes are drilled into the PDMS using a borer to produce inlets and outlets. Finally, PDMS can seal to itself and other flat surfaces irreversibly since both surfaces are Si-based materials and have been oxidized by plasma before contact (a process that forms a covalent O-Si-O bond). Seals are watertight and can be formed under ambient conditions (unlike silicon and glass, for which bonding requires high temperatures or adhesives) (Figure 4.4).

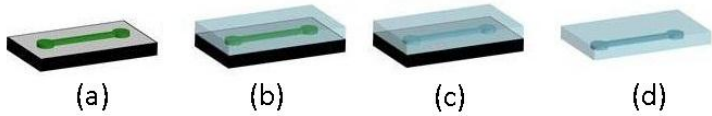

Figure 4.4 Production step of a microfluidic device: creation of the mold (a); pouring (b) and polymerization (c) of PDMS; (d) removal of the master.

If desired, many PDMS replicas can be made from a single master. This procedure of producing the PDMS structure from the silicon master,

called replica molding, can be carried out in clean room, and can replicate certain types of features with dimensions down to 10 nm.

5. MORPHOLOGICAL CHARACTERIZATION OF BIOLOGICAL SAMPLE VIA DHM

The evaluation of sperm morphology is an important task in the assessment of semen quality. By means of this evaluation, it is possible to verify the integrity of spermatozoa structures involved both in movement (the tail) and fertilization, in terms of penetration and activation of oocyte (acrosome). Therefore, sperm morphology is regarded as a significant prognostic factor for fertilization (4), as abnormal sperm morphology is one of the most common factors of male infertility. For this reason in the past years, several techniques have been developed in order to analyze, in greater detail, the morphological alterations of spermatozoa in their nearly physiological environment. Most of these techniques commonly used to obtain such information involve biochemical processes that require specific laboratories and may alter the vitality of the sperm analyzed. On the other hand, spermatozoa appear essentially transparent under bright-field microscope, unless either optical-contrast interference microscopy (differential interference contrast (DIC) configuration) is used, or the specimen is stained and fixed (6), a process in which the level of repeatability heavily depends on the experience of the technician and environmental conditions (such as, temperature, pH level, and duration); furthermore, the staining treatment strongly reduces the vitality of the cells making them useless for insemination (7). Finally, by optical microscopy, it is difficult and time-consuming to obtain a quantitative morphological imaging of the spermatozoa under test. In fact, a fine z-movement of the biological sample is required in order to acquire a collection of different planes in focus. This collection of acquired images is used in post-elaboration to produce a 3-D image of the object under investigation. Some improvement can be achieved by using an atomic force microscopy (AFM) (8) (9), where the morphological information of the sample is obtained by raster scanning the sample under a sharp contact probe that is deflected by changes in sample thickness (z height). The position of the sample is adjusted to maintain a minimal set point deflection of the cantilever and these adjustments are used to generate a topographical map of the

spermatozoa. However, the raster scanning could be time-consuming limiting real-time characterization of the biological sample. Moreover, the cost of the technique makes its use in zootechnical industry not encouraging.

In this chapter, the effectiveness of digital holography microscopy (DHM) as a technique to obtain quantitative analysis of bovine sperm is demonstrated. In particular, the estimated informations, about the dimensional and morphological parameters of animal sperm, and the user-friendly format of the results prospect the DHM as an adequate technique for prognostic fertilization based on morphological analysis, in zootechnical industry. All the results showed in the present chapter have been acquired with a Fully Coherent DHM.

5.1 Description of the sample

The morphological analysis proposed in this chapter has been dedicated both to bovine and human sperm cells. The first activity has been performed in collaboration with the institute "L. Spallanzani" in Milan, the second with the Centre for instrumental insemination CFA-IFAHealth, directed by Prof. Brian Dale in Naples.

5.1.1 Bovine sperm cells

In Figure 5.1, DIC image of a bovine sperm head is reported, where both the tail and the head are visible. The tail is composed of the neck, middle, principal, and end pieces and is responsible of sperm motility, necessary to the spermatozoon to reach the oocyte (36). The head, which has dimensions of about 5 μm × 10 μm and an height of about 0.50 μm, allows the fertilization in terms of penetration and activation of oocyte (acrosome). The acrosome is a thin, double-layered membrane sac that is closely applied to the anterior end of the sperm nucleus during the last stages of sperm formation. This cap-like structure contains several hydrolytic enzymes that are used by the spermatozoon to disperse the corona radiate and to pass through the zona pellucida of the oocyte. The bovine sperm cells to be analyzed by DHM were prepared by the Institute "Lazzaro Spallanzani" after fixation in suspension of the seminal material with 0.2% glutaraldehyde solution in phosphate buffered saline (PBS) without calcium and magnesium (1:3 v/v). A drop with volume 6 μL has been deposed on a

glass slide, and then, covered with a cover slip (20 mm × 20 mm). The cover slip has been linked to the glass slide by means of a strip of varnish.

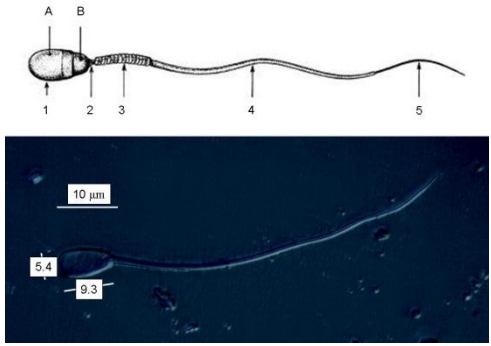

Figure 5.1 (Upper side) Structure of the spermatozoon: (1) head, (2) neck, (3) middle piece, containing the mitochondrial sheath, (4) tail, and (5) end piece. The male gamete's head is partially covered by (A) acrosome [26] and (B) the remaining part is named as postacrosomal region. (Lower side) Image of a bovine spermatozoon obtained by an optical-contrast interference microscope

5.1.2 Human sperm cells

The human spermatozoon is a polarized motile cell, which delivers the haploid male genome to the oocyte, introduces the centrosome and triggers the oocyte egg into activity.

The head contains three functional parts; the nucleus with a haploid set of chromosomes, in which deoxyribonucleic acid (DNA) is packaged into a volume that is typically less than 10% of the volume of a somatic cell nucleus (37) (38); the acrosome, a large Golgi-derived secretory vesicle on the proximal hemisphere of the head containing an array of hydrolytic enzymes necessary for digesting the zona pellucida during penetration (39) (40); and the perinuclear theca, a rigid capsule composed of disulfide bond-stabilized structural proteins amalgamated with various other protein molecules (41). Human spermatozoa have been shown to exhibit a wide range of head shapes. A number of studies

indicate that sperm morphology best predicts of outcome for natural fertilization (42), intra-uterine insemination conventional IVF and ICSI (43).

Nuclear vacuoles have been described as a crater defect in the spermatozoa of stallion, as a crater defect, a pouch formation, a diadem defect or a nuclear sperm defect in bull spermatozoa, and as a crater defect or a pouch formation in boar spermatozoa. The defect is believed to originate during spermatogenesis as vacuoles have been found in both early and late spermatids. Nuclear vacuoles were shown by electron microscopy to be narrow-mouthed invaginations of the nuclear membrane into the nucleoplasm (44). The appearance of these 'nuclear pouches' in bull spermatozoa forming a string at the site of the acrosome postacrosomal sheath junction gave rise to the name 'diadem defect'. The predominant locations of the vacuoles are the apical region and the acrosome-postacrosomal sheath junction but they have also been found throughout the sperm head (44).

Ejaculates were collected by masturbation from 15 male scheduled to undergo IVF at the Centro Fecondazione Assistita (CFA), Naples. After liquefaction, 0.5-1.0 ml of each specimen was processed using a double-density-gradient centrifugation method (Percoll, Sydney IVF). The final pellets were resuspended in Ham's F-10 (Gibco) and used to prepare slides for DESA. Briefly, a semen aliquot containing 2x106 spermatozoa was washed 2x by centrifugation with phosphate-buffered saline (PBS). Then the pellet was suspended in 100 µl of 2% formaldehyde in PBS and fixed for 10 min. at room temperature. A 10 µl aliquot was then spotted onto a clean microscope slide, allowed to air dry and mounted with PBS:Glycerol (1:1) (v/v).

In order to study the single cells by both Digital Enhanced Sperm Analysis (DESA) and DHM, a grid of 20x20 circles (with a radius of 100µm) was placed over the microscope slide. This grid was made by a photolithographic process that allows the transfer of the shape of the grid from a mask to a photo-sensitive polymer. At the end of this process, the whole surface of the slide was covered with a 1µm-thick photo-sensitive material except the circles. A 10 µl aliquot was than spotted on the grid and finally a cover slide was placed to seal all. Only cells that fell in the circles of the grid gave results.

Slides were first examined under immersion oil using an inverted microscope (TI-DH; Nikon Instruments Italia) equipped with Nomarski optics enhanced by digital imaging to achieve a magnification of up to X 1500. The images were captured by a colour video camera for high-quality image production and analysed using image processing software (NIS-Element Documentation, Nikon).

5.2 Phase reconstruction of bovine sperm cell in air and in their native environment

In the present paragraph results relative to phase map retrieval for bovine sperm cells in air and human sperm cells in their native environment will be presented. For the first case the LSI algorithm (29) will be used while for the second experimental situation double exposure procedure (28) has been performed.

DHM has been employed to evaluate the morphology of bovine sperm cells order to verify the integrity of their structures. In this section, a set of different images, is reported. In Figure 5.2(a), the image of an acquired hologram is reported, whereas its inset shows the intensity of the fringe pattern due to the superimposition of the object and reference beam. In Figure 5.2(b), a pseudocolor plot of the unwrapped phase-contrast map reconstruction of a bovine spermatozoon is reported. The color bar reports the value in radians of the phase difference. For this map, the difference between the minimum and the maximum is about 1.7 rad. For the reported analysis, the spermatozoa are fixed and the measurements shown in the following have been performed in a region of the sample in which no liquid is surrounding the cell. In (3.37), the OPD can be evaluated as the product between the thickness of the spermatozoa and its refractive index (45). A quantitative information about the thickness of the sample under test is obtained by (3.37), by considering an uniform refractive index of about 1.35. The refractive index of the sperm cells has been estimated from the reconstructed phase maps by means of the value of the maximum thickness of bovine sperm cells, as reported in (46), i.e., 0.50 μm. From this information, we calculated the value of the refractive index when the OPD is in its maximum for several reconstructed phase maps and, averaging the calculated values, the refractive index of the cells was estimated. Figure 5.2(c) illustrates the quantitative reconstructed

morphology obtained by applying (3.37) at the phase-map contrast. The resulting error on the thickness of the cells, considering a refractive index for the sperm cell of 1.35, is ±11 nm.

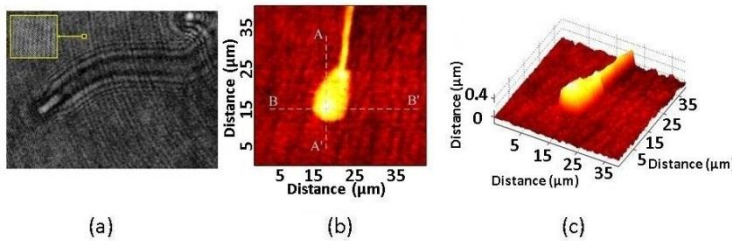

Figure 5.2 (a) Acquired hologram, a region is enhanced in order to show the interference pattern (inset). (b) Pseudocolor plot of a phase-contrast map for a bovine spermatozoon. (c) Pseudo 3-D representation of the thickness of a bovine spermatozoon obtained by DHM.

It is worthnoting that this 3-D image is obtained from the reconstruction of a single acquired hologram, which is without the use of any mechanical scanning. The great advantage to manage quantitative information allows carrying out different numerical analysis (such as, estimation area, profiles along particular directions, and selection of different zone) that can improve the understanding of the relationship between the abnormal morphology and the male infertility. In particular, in Figure 5.3(a) and (b) are reported the quantitative profiles of the spermatozoon morphology along the lines AA' and BB' illustrated in Figure 5.2(b), respectively. Finally, in Figure 5.3(c), as example, isolines relative to five different thicknesses of the sample (i.e. [0.30, 0.35, 0.40, 0.45, 0.50] μm) and individuated by the contour function of Matlab are displayed. Then, for each region defined by the isolines the occupied area and the relative volume has been numerically estimated and the carried out values are reported in tab. I. The inaccuracy committed in the estimation of the area and of the relative volume for each region is mainly due to the cited error in the evaluation of thickness.

In the next set of images the DHM approach has been employed to obtain high resolution images of morphological alteration (47).

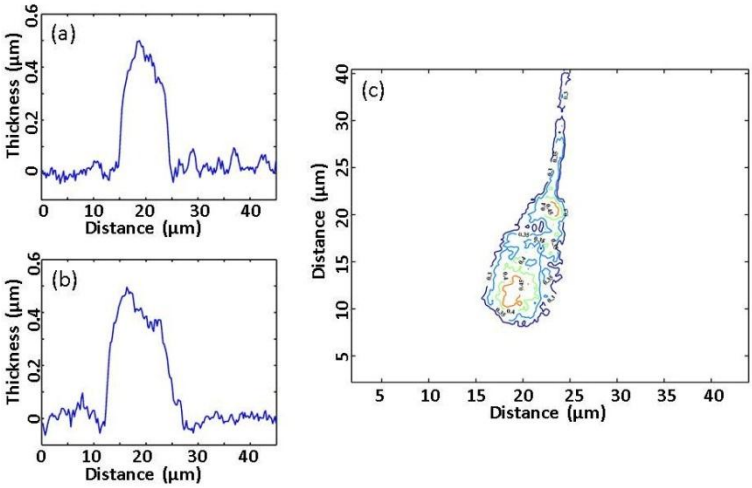

Figure 5.3 (a) and (b) profiles plot along the lines AA' and BB' reported in Figure 5.2 (b). (c) Isolines relative to five different thicknesses of the reconstructed image.

TABLE I

Reference Thickness (µm)	Calculated area [µm× µm]	Calculated volume [µm× µm × µm]
0.30	73.7	27.9
0.35	51.8	20.7
0.40	24.4	10.5
0.45	3.5	1.62

In particular, in Figure 5.4(a) the reconstructed image of a spermatozoon with a cytoplasmatic droplet along the tail is reported. Cytoplasm surrounding the sperm cell is accumulated during maturation and in the last phases of the process is extruded from the cell. Cytoplasmatic residues may however persist in the cell as a droplet and are retained in the tail. When droplet is located in the neck region this defect is defined as "proximal droplet", while when the defect involves the middle piece is known as "distal droplet" (36). Thus, the presence of drops along the tail is connected to the degree of cell maturation and may indicate an excessive utilization of a donor.

In Figure 5.4(b) a reconstructed image with a bent tail sperm cell is displayed. This defect can be associated with low sperm motility. When is present in the semen either before and after the freezing process, this defect underlines a reproductive problem of the donor. When this anomaly appears with high frequency only in frozen semen, it can indicate that the spermatozoa have been subjected to hypo-osmotic stress possibly due to an improper use of freezing extender and to an extremely low concentration of solutes.

In Figure 5.4(c) a sperm with broken acrosome is displayed. This defect is not common in fresh semen but it can be present with high percentage in frozen semen samples. The loss of acrosomal substances indicates a premature acrosome activation far from the site of fertilization. This defect is usually due to incorrect sperm handling during the freezing process.

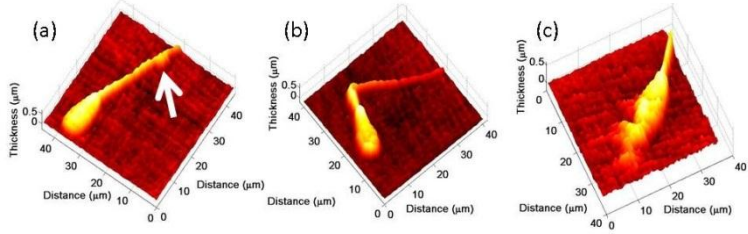

Figure 5.4 Pseudo 3D representation of the thickness of a spermatozoon with: (a) a cytoplasmatic droplet along the tail; (b) a bent tail; (c) an acrosome broken.

Finally, Figure 5.5(a) a reports an interesting image, common to many spermatozoa analyzed, showing a “protuberance” on the post-acrosomal region of the head. This alteration is well-visible in the profile reported in Figure 5.5(b) and relative to the line AA' shows in the inset. This particular formation, in our knowledge, has never been highlighted by optical microscopy. Among possible explanations of its nature, an artifact due to a possible different refractive index between the post-acrosomal region, (containing almost exclusively highly compact chromatin) and the acrosome should be excluded.

In fact, this characteristic has been also observed in images provided by confocal DCM 3D Leica microscope (see Figure 5.5(c)). In particular, Figure 5.5(c) is obtained by a software elaboration of a stack of about

40 images relative to different distance between the sample and a 150X (NA=0.95) microscope objective. As it can be noted, the quantitative information obtained with the Leica Microscope are comparable with the information reconstructed by the DHM approach, with the great difference that in the latter case the reconstruction process requires just a single acquired image (i.e the hologram).

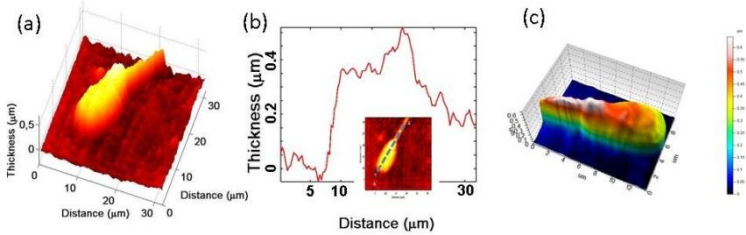

Figure 5.5 (a) Pseudo 3D representation of the thickness of spermatozoa with abnormal "protuberance". (b) Profile of the head along the line AA' illustrated in the inset; (c) Data obtained by the confocal DCM 3D Leica microscope.

A first explanation for the estimated area and volume variation is that the protuberance highlighted by DHM could be due to the presence of the centrioles into the structures connecting the tail to the head. However, in order to give a correct biological explanation to the origin of this formation, more detailed analyses are required.

The reported discussion should have clarified the additional benefits of DHM phase contrast imaging in comparison to DIC imaging. By means of the DIC microscopy a 2D reconstruction of the shape of the cells can be reconstructed, which is very poor in terms of quantitative information unless a phase-shifting module is added into the DIC set-up. However, by a DIC with a phase-shifting module, multiple images have to be digitized in order to obtain "quantitative information". DHM instead allows us to reconstruct the quantitative phase map from a single hologram, a single image needs to be recorded, and as it clear that is a relevant advantage in case of live objects. In any case, each value of the matrix forming the DHM phase map represents the phase delay of the light passing through the sample which is connected with the thickness of the cell. This kind of information is purely quantitative

and can be simply used for the morphological analysis of the cells and for the selection of the anomalies (48).

Human sperm cells in their native environment have been then reconstructed. A total of 2000 digitilized sperm heads were analysed for six primary parameters (area, perimeter, length, width, number and size of vacuoles). DESA analysis revealed that the mean values for length, width, area and perimeter of the sperm head were 5.2 ± 0.6μm (range: 3.6 to 7.9), 3.5 ± 0.4 μm (range: 2.4 to 5.6) 14 ± 3 μm^2 (range: 7 to 26), 13.7 ± 1.4μm (range: 9.6 to 19.7). In the fifteen ejaculates 62.8% of spermatozoa with one or more vacuoles were found. The number of vacuoles per sperm ranged from 0 to 8 (mean: 2.0 ± 1.8) measuring 0.03-5.90μm^2 in area (Figure 5.6).

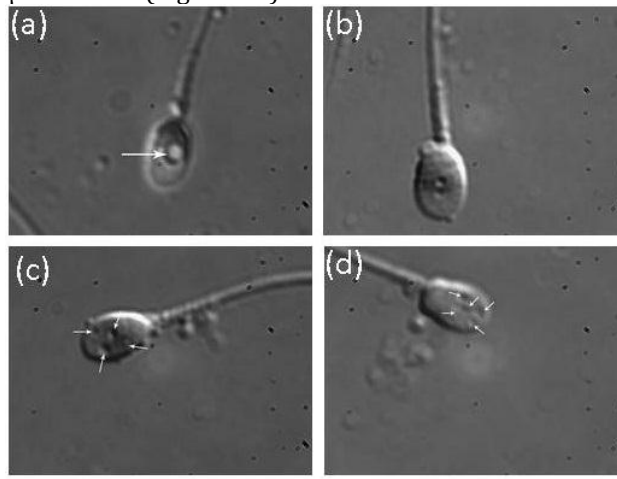

Figure 5.6 High-power light microscope micrograph of sperm heads (1500X). (a) crater-like appearance of nuclear vacuoles: (b, c, d) Spermatozoa with one or more vacuoles.

We used DHM to evaluate the morphology of 200 of the above spermatozoa (Figure 5.7). in order to verify the integrity of their structure. Figure 5.7 shows a set of different images, reconstructed according to the procedures described above. In Figure 5.7(c) a pseudocolor plot of the phase-contrast map reconstruction of a human spermatozoon is reported. The colour-bar shows the value in rad of the

phase difference which depends on the optical density and thickness of the biological sample.

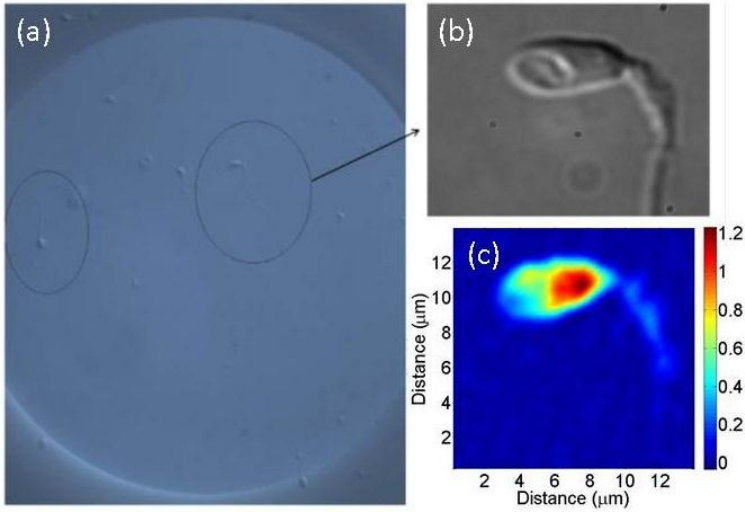

Figure 5.7 (A) A circle of a grid of 20x20 circles (with a radius of 100μm) placed over microscope slide. (B) Differential interference contrast micrograph of a sperm head. (C) Pseudocolor plot of the same spermatozoa.

It is important to point that this three-dimensional allows us to carry out different numerical analyses, such as an estimation of area, profiles along particular directions and selection of different zones. In Figure 5.8(c) and (d) we show the quantitative profiles of the spermatozoon along the lines AA' and BB' illustrated in Figure 5.8(a), respectively. These profiles show, point by point a quantitative value of the phase shift due to spermatozoon structure. This information may be useful both to note qualitative and quantitative variations. Quantitative phase shift information from DHM allows us to calculate more accurately the volume/mass of the sperm head. In Figure 5.8(b), for example, an isoline plot relative to different height of the sample is displayed. For each region defined by the isolines, the occupied area and the relative volume can be numerically estimated. This approach may be applied to a large number of specimens and may provide a useful tool for semen quality evaluation.

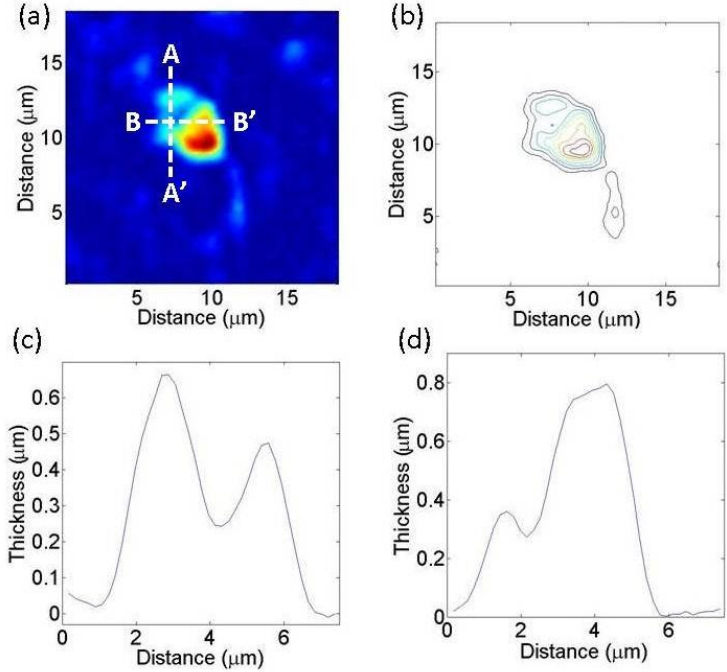

Figure 5.8 (a) Pseudocolor plot of a phase-contrast map for a human spermatozoon; (b) Isolines plot of the reconstructed spermatozoon image; Profile plot along the lines (c) AA' and (d) BB'.

In Figure 5.9 we show a quantitative comparison between a control spermatozoon and a spermatozoon with vacuoles. Figure 5.9(a) and (b) illustrate the height profile along the major axis of the sperm head for the defect-free spermatozoon and the spermatozoon with vacuoles, respectively.. It's worth to note that both the shapes and the point by point value of the height are different. In particular, the spermatozoon with vacuoles has a distinct depression in the profile (see the arrow in the figure). Moreover, its major axis appears longer than that of the normal spermatozoon. On the other hand, the profile of the normal spermatozoon results higher than that of the spermatozoon with

vacuoles. These differences may be due to surface variations and/or variation of the inner structure of the sperm head.

In Figure 5.9(c) and (d), the contour maps of the two spermatozoa are shown. Contour lines of these maps are relative to four different heights of the sample (i.e., 0,10, 0.50, 0.70, and 0.90 μm). For each region defined by the contour lines, the occupied area has been numerically estimated, and are reported in Table II. Both the contour map and values reported in Table II show the presence of a depression in the head sperm.

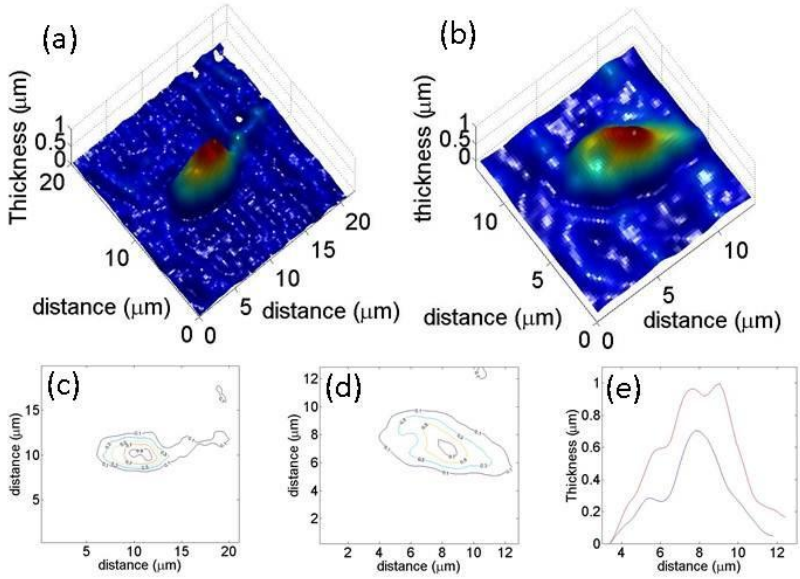

Figure 5.9 Comparison between a defect-free spermatozoa and a spermatozoa with vacuoles.

This approach opens the possibility to use DHM as an in-vivo technique for a more complete sperm analysis without altering their viability. The proposed technique can be considered a valid alternative method for the investigation of morphological features and the sorting of the motile sperm cells (49).

TABLE II

Reference Thickness (μm)	Calculated area in presence of a vacuole [μm× μm]	Calculated area in absence of a vacuole [μm× μm]
0.1	26.48	34.41
0.3	12.62	17.89
0.5	4.78	11.69
0.7	0.97	6.42
0.9	0	1.82

5.3 Phase reconstruction of sperm cells flowing in a microchannel

The analysis carried out in the previous section are relative to spermatozoa fixed on glass slide for optical microscope. However, DHM provides the advantage of directly observing spermatozoa in their native environment. For this aim a micro-systems with fluidic channels in PDMS has been fabricated (35). The liquid containing the bovine sperm to analyse entries into the channels for capillarity. In a Figure 5.10(a) an optical image obtained by an optical contrast interferometric microscope with an objective 20X (NA=0.4) of a spermatozoon into a channel is reported; whereas in Figure 5.10(b) the reconstructed phase-contrast map obtained by DHM is shown. In order to obtain this image a double exposure technique has been performed. In fact the LSI technique cannot be used in presence of microchannels, since the integrating procedures fail in presence of the background jump. In particular, the first acquired hologram was relative to the microfluidic channel full of liquid but without spermatozoa. Thanks to the movement due to the capillary effect, the second hologram was acquired when the spermatozoon crossed the channel in the field of view of the CCD camera. This approach allows to eliminate both the contribute due to the channel and aberrations due to the glass slide and the liquid that contains the spermatozoa. However, some “track” of the channel is still visible in the reconstructed images (see dashed lines). As it can be noted, the phase-contrast map is lower than the phase-map contrast obtained with the spermatozoa fixed on the glass slide. This can be explained by the minimum difference between the refractive index of spermatozoa and the surrounding liquid. More accurate images

require an improvement in the DHM technique, and to achieve this target we developed the approach presented in the following section (48).

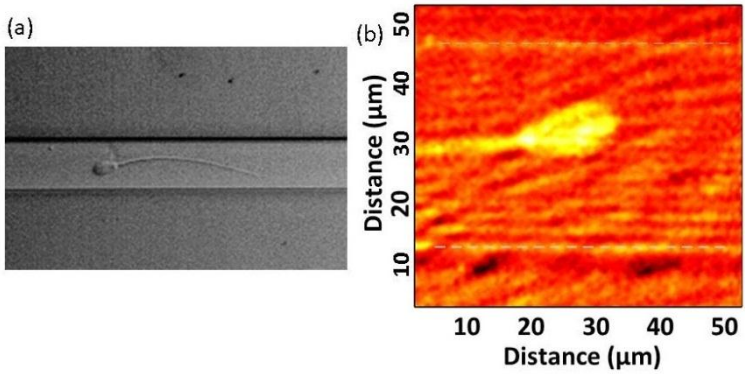

Figure 5.10 (a) DIC image of a spermatozoon into a microchannel. (b) Reconstruction image of a spermatozoon.

5.3.1 Digital self-referencing quantitative phase microscopy by wavefront folding

In microfluidic channels, the flat area surrounding the channel is very wide (compared to the channel area), and the object wavefront can be used to obtain self-referencing interferometry, as was recently demonstrated by Jang et al. (50). The Jang setup allows creating an interferogram between the original object wavefront and its mirror replica. This replica was obtained by a fine optical adjustment and alignment of a microscope objective added into an additional arm of the DH setup. The two wavefronts interfere in such a way that a flat area is superimposed to the area occupied by the microfluidic channel with the biological specimen. This approach has been demonstrated to be valid for reconstructing quantitatively the phase distribution of different specimens. Nevertheless, the method described in (50) requires both an appropriate setup and two-dimensional (2D) weighted polynomial fitting. In this paragraph we show that, by taking advantage of the possibility offered by DH to numerically manage the reconstructed complex wavefronts, a novel and full numerical approach can be adopted to get QPMs. The method is based on the generation of a

numerical replica of the original complex wave field. To obtain the desired QPM, the replica is digitally shifted and the corresponding phase is subtracted from the original wavefront. Our approach can be explained as a wavefront folding, which allows superimposing the portion corresponding to a flat region on the region in which the object under investigation lies. Compared to the method reported in (50), which can be considered a true self-referencing optical setup, in our approach the replica is obtained numerically and for this reason was named "digital self-referencing." Moreover, a standard Mach–Zehnder setup has been used, whereas in (50) a Michelson configuration was adopted. The effectiveness of the our method has been proved for different objects. A microfluidic channel, 20 μm wide and 10 μm high, was fabricated by standard PDMS procedures (35). Liquid containing the bovine sperm has been injected inside the channels by the capillarity effect. The phase-map distribution in presence of the spherical aberration (Figure 3.7) can be described trough the discrete representation

$$\phi(n,m) = \phi_0(n,m) + i\frac{k}{2R}[(n-N_0)^2 + (m-M_0)^2] \quad (5.1)$$

for k =2π/λ, n = 1,…, N, and m = 1,…, M, $\varphi_0(n,m)$ is the digitalized phase distribution of the object under observation, N and M are the dimensions of the pixel matrix, while the quadratic term takes into account the curvature, with a radius of R, introduced by the microscope objective. The parabolic term is centered on the pixel with coordinates (N_0, M_0). In Figure 3.7, it is clear that the large phase retardation due to the microscope objective hides the thin phase contribution of the specimen. To retrieve the correct phase, a portion of the wavefront, where the contribution of the observed object is null, is identified and selected. This portion can be used as reference phase map since it corresponds to a flat region with a constant and uniform phase. A numerical replica of the wavefront is obtained by laterally shifting the original wavefront; in this way a reference phase map φ_{ref} is generated. In particular, the obtained self-referencing map can be described by

$$\phi_{ref}(n,m) = i\frac{k}{2R}[(n-N_0+\Delta N)^2 + (m-M_0+\Delta M)^2] \quad (5.2)$$

for n = N_1,..., N_N and m = M_1,..., M_M , where (N_N − N_1) and (M_M − M_1) define the dimensions of the region of interest relative to the object. ΔN (ΔM) is the amount of shift along the x (y) direction needed to superimpose the selected portion on the region where the object is present. The difference between φ and φ_{ref} gives the following equation

$$\phi(n,m) - \phi_{ref}(n,m) = \phi_0(n,m) - i\frac{k}{R}\left[\Delta N\left(n - \left(N_0 - \frac{\Delta N}{2}\right)\right) + \Delta M\left(m - \left(M_0 - \frac{\Delta M}{2}\right)\right)\right] \quad (5.3)$$

n = N_1,..., N_N and m = M_1,..., M_M. The second term on the right-hand side of the above equation is a linear phase term that can be easily removed by a linear 2D fitting. The aforementioned procedure for retrieving the QPM of the spermatozoa in a microfluidic channel is illustrated in Figure 5.11.

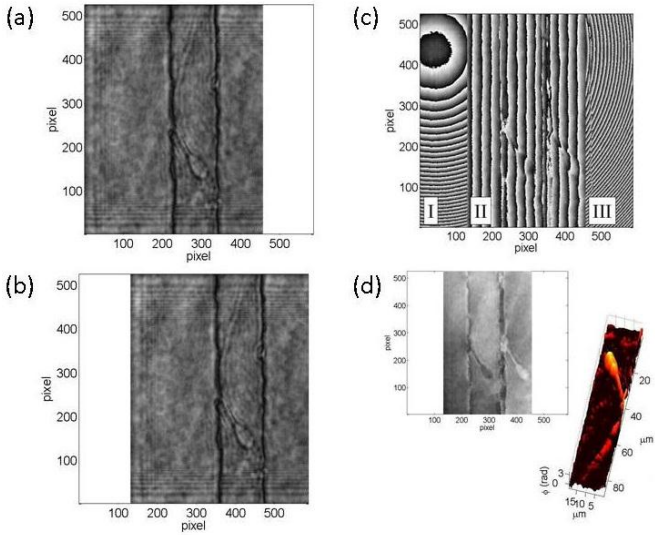

Figure 5.11 The reconstructed in-focus intensity map of (a) the original wavefront and (b) its shifted replica.(c) Phase map obtained subtracting the phases of the original wavefront and the shifted replica. (d) The 2D and the

pseudo-3D unwrapped phase map after the elimination of the superimposed plane

The intensity image of the object from the original reconstructed wavefront is shown in Figure 5.11(a), while the shifted replica is shown in Figure 5.11(b). The subtraction between the phases of the original wavefront and its shifted replica is shown in Figure 5.11(c). The regions I and III correspond to the phase map of the quadratic term introduced in (5.1) while region II is the wrapped phase distribution of both the spermatozoa and a superimposed linear carrier (5.3). Because of the shifting, the region with the spermatozoa has been duplicated. A 2D linear fitting is used for removing the superimpose plane; moreover, the averaging of the duplicated regions with the spermatozoa permits increasing the signal-to noise ratio. Finally, the unwrapped phase map of the object is obtained, as shown in Figure 5.11(d). Region II consists of different subregions separated by the channel's boundaries. To take into account the discontinuities, a 2D weighted polynomial fit could be used to unwrap simultaneously the phase in all of region II. However, it is important to note that we used a linear fitting for obtaining the unwrapped phase in each of the rectangular areas inside the dotted lines in Figure 5.11(d).

In summary, the proposed method allows a digital self-referencing quantitative phase reconstruction by recording a single hologram and without modifying the standard off-axis DH experimental setup. The proposed method is suitable for structures in which the object under investigation is surrounded by a large flat region such as a microchannel devices (51), (52) .

6. AUTOMATED 3D TRACKING

The detection and the tracking of micrometric particles, such as bacteria, cells or marine microorganism, is an important task for the evaluation of biological parameters. Special relevancy is associated to the knowledge related to the motility, i.e. curvilinear and linear velocity, wobble etc. We propose an approach for the detection and the three dimensional tracking of a Giardia flowing in a microfluidic channel, acquired with a partial spatially coherent DHM, Paramecia and human sperm cell moving in a free 3D space, acquired with a fully coherent DHM. The developed algorithm can be simply applied to spermatozoa fertility evaluation.

6.1 Description of the sample

In the following paragraphs three different types of particle have been used in order to develop the tracking algorithm. The simplest evaluate case has been an alga flowing in a microchannel, thus experiencing mainly an XY displacement, in the framework of the collaboration with the MRC-ULB. In the following, paramecia moving in a free 3D space have been tracked, where the problem of the background cleaning and the multiple particles tracking has been solved. In the end the algorithm has been applied to the case of human sperm cells, in the framework of the collaboration with the CFA.

6.2 Alga flowing in a microchannel

Giardia lamblia (synonymous with Giardia intestinalis, Lamblia intestinalis and Giardia duodenalis) is a flagellated protozoan parasite that colonizes and reproduces in the small intestine, causing giardiasis (Figure 6.1). The giardia parasite attaches to the epithelium by a ventral adhesive disc, and reproduces via binary fission. Giardiasis does not spread via the bloodstream, nor does it spread to other parts of the gastro-intestinal tract, but remains confined to the lumen of the small intestine. Giardia trophozoites absorb their nutrients from the lumen of the small intestine, and are anaerobes. If the organism is split and stained, it has a very characteristic pattern that resembles a familiar

"smiley face" symbol. Chief pathways of human infection include ingestion of untreated sewage, a phenomenon particularly common in many developing countries; contamination of natural waters also occurs in watersheds where intensive grazing occurs. This microorganism has been acquire while flowing in a microchannel of dimensions, using a partial spatially coherent source (par. 4.1.2).

Figure 6.1 Giardia lamblia.

6.2.1 Detection of XY via the area and the convolutional approach

A set of 123 holograms of a Giardia flowing in a channel (largeness 120 μm, depth 80 μm), with a frame rate of 15 acquisitions for second, have been acquired and the resulting phase map have been evaluated.

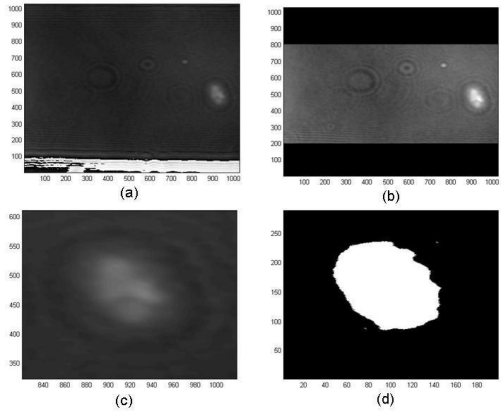

Figure 6.2 First Procedure for detection.

In the compensated phase map of the first acquisition (Figure 6.2(a)) the border region has been removed by means of a mask (Figure

6.2(b)). By using the Otsu's method the threshold is evaluated and, after the selection of the region of interest (ROI, Figure 6.2(c)) the area (measured as # of pixels) is evaluated (Figure 6.2(d)). This area is then used as reference for the automated detection of the object's position in the following flux images. In fact for each hologram the Otsu's thresholding is performed, the image is segmented in its composing parts and the area of each segmented part is compared to the reference area detected previously. The region whose area is closer to the reference value is chosen as the one in which the cell is present. The possible presence of an above-threshold region connected to the image border is automatically removed in order to avoid the possibility of finding false positives in the cell detection procedure (Figure 6.3).

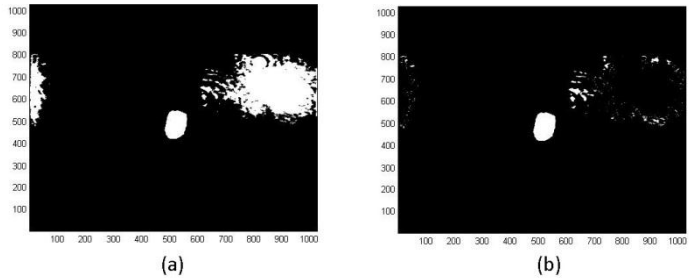

Figure 6.3 Border cleaning procedure.

Otherwise a convolutional approach can be used for the XY detection. The correlation function between the selected object and the whole compensated phase map is evaluated. The central position of the cell corresponds to the maximum value of the correlation function (Figure 6.4(a)). The little structure in bright blue present on the top-left of the cell is in correspondence of the particle visible, in the same position, in Figre 6.2(a). Because of the different dimension, the correlation in this case is much lower. The position is recorded as the X and Y coordinates of the cell. The orientation (defined as the angle between the x-axis and the major axis of the ellipse circumscribing the above-threshold pixels) of the cell is recorded as well. Results are shown in Figure 6.4(b-c).

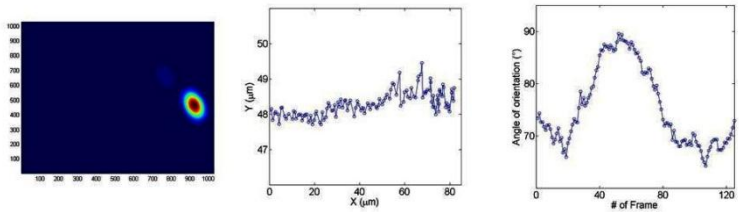

Figure 6.4 (a) Correlation function between the reference object and the whole image; (b) XY position of the cell and (c) unwrapped angle of orientation of the cell in motion.

In the following step the Z position (focus distance) is evaluated.. The selfocusing function (SFF) described in (30) is then defined. In order to avoid a time consuming calculation of the SFF in the whole range of possible reconstruction distances and to overcome the limit of a chosen step for the evaluation of the SFF, an algorithm looking for the minimum of a function within a fixed interval has been used. The sign of the SSF is inverted since it has to be maximum in the focus plane of a phase object. Reasonably the resolution of hundredth of micron for the evaluation of the focus plane distance (Z) has been chosen. The criterion is repeated for the whole set of flux images and the resulting values are plotted in Figure 6.5. The high change of position in Z is compatible with the focalization's degree of the particle in the corresponding images.

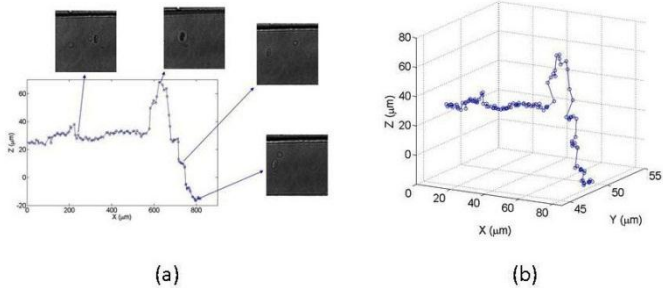

Figure 6.5 3D tracking of the Giardia.

6.3 Paramecium moving in a free 3D space

Subsequently the same technique has been applied to a Paramecium moving in a free space. The dimension of this objects is about tenth of μm. The acquisition have been performed using a fully coherent DH setup at the Laboratory of the IMM-CNR in Naples. The hologram acquired are thus appreciably more noisy of the previous one, both for the fully coherent nature of the light, both for the thickness of the sample (about 2 cm) composed by water, paramecia and suspended vegetable waste acting as diffusion source. For the magnification of the sample a 20× microscope objective has been used.

6.3.1 Background cleaning thought the difference of two following acquisitions

Because of the noisy background an equalization procedure have been performed. In particular the average of all the phase maps has been evaluated and it has been used as a background to remove by means of the relation:

$$\phi_{Eq} = \frac{\phi - \phi_{mean}}{\sqrt{\phi_{mean}}} \quad (6.1)$$

being ϕ the phase to be equalized (Figure 6.6(a)), ϕ_{mean} the background obtained by means of the average evaluation (Figure 6.6(b)) and ϕ_{Eq} the equalized phase (Figure 6.6(c)).

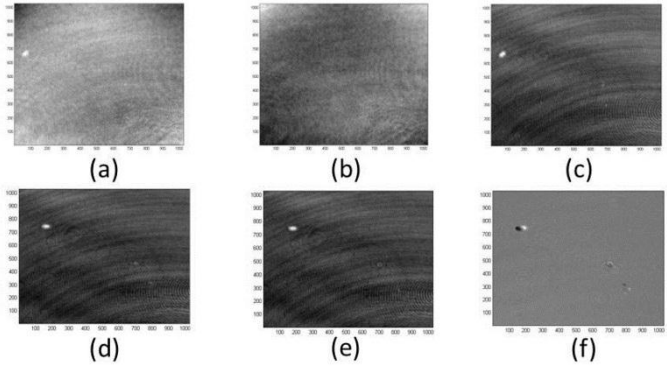

Figure 6.6 Background removal via equalization (a) and difference of two following acquisitions.

Another solution proposed to remove the background noise consists in subtracting two following phase maps (Figure 6.6(d-f)). The black and the white spots correspond to the position of the paramecium in the phase map (d) and (e) respectively. After the detection of the 3 coordinates XYZ the phase maps and the related path have been mounted together in a video. The result of the tracking is shown in Figure 6.7.

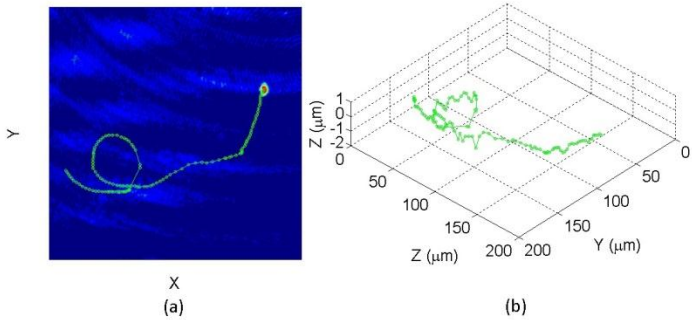

Figure 6.7 Single particle tracking: XY (a) and 3D(b).

6.3.2 Contemporary tracking of multiple particles

Subsequently the procedure have been applied for the tracking of multiple particles, where the procedure applied to the whole phase map failed making confusion between the different particles. Thus a proximity criterion has been developed, in which the position in the (n+1)-th frame have been looked for in a reasonable neighborhood of the n-th frame position.

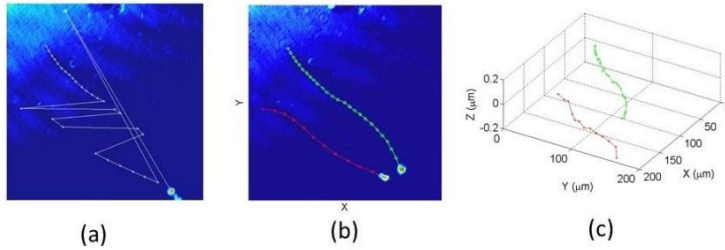

Figure 6.8 Application of the tracking algorithm without (a) and with (b) the proximity criterion.

The result of the proximity correction of the tracking procedure is reported in Figure 6.8(c). It is interesting to notice that the two objects are moving on different planes while, from a XY point of view, they are apparently crossing each other.

6.4 In-vivo tracking of a human sperm cell

The algorithm has been applied to the tracking of human sperm cells, in the framework of the collaboration with the CFA-IFAHealth. Sperm ejaculated outside the body may survive only few hours and the analysis has been performed while cells were still alive. The algorithm has been applied to highlight the behaviour of an anomalous sperm cell. In particular the cell showed a non-linear movement since the bent tail anomaly was present (Figure 5.4(b)). Again for the magnification of the sample a 20× microscope objective has been used. In the following figure, the result of the tracking is showed.

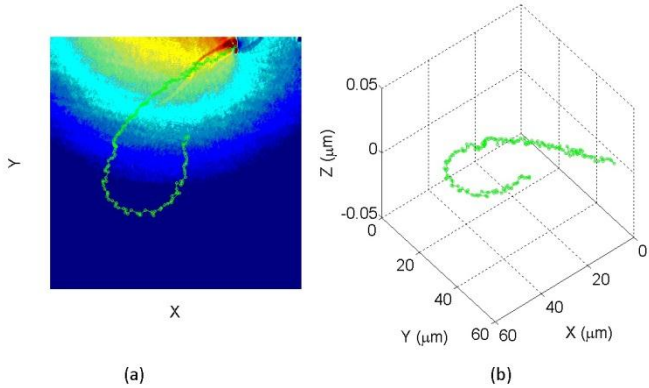

Figure 6.9 Human sperm tracking, XY (a) and 3D point of view (b).

7. CONCLUSIONS

The research activity presented in this thesis has been devoted to the setting up of a Digital Holographic Microscope, compatible with micro-manufactured devices (such as micro-channels), and to the development of the numerical algorithm aimed at the retrieval of the needed biological parameters. One of the main advantages of DH is that a high-resolution 3-D quantitative sample imaging can be automatically produced by numerical refocusing of a 2-D image at different object planes without any mechanical scanning (45). Moreover, using a single acquired image is possible both to reduce the size of the mass storage devices required for images saving and to achieve a fast image transfer. High-resolution images of bovine sperm have been obtained by DHM from the reconstruction of a single acquired hologram. The great advantage to manage quantitative information allows carrying out different numerical analysis (such as, estimation area, profiles along particular directions, and selection of different zone) that can improve the understanding of the relationship between the abnormal morphology and the male infertility. DHM approach has been also employed to obtain high-resolution images of morphological alteration. DHM provides the advantage of directly observing spermatozoa in their native environment. For this aim, a microsystems with fluidic channels has been fabricated. In particular, polydimethylsiloxane (PDMS) has been employed to realize the microfluidic system and microchannels have been obtained using soft lithography procedures, and they have been sealed with a Corning glass by means of a bonding process. In particular, microchannels have a rectangular section with a width of about 20 μm and a height of about 10 μm. Initially the reconstruction of the phase map of the cell has been obtained by a double exposure technique. In particular, the first acquired hologram was relative to the microfluidic channel full of liquid, but without spermatozoa. Due to the movement caused by the capillary effect, the second hologram was acquired when the spermatozoon crossed the channel in the field of view of the CCD camera. This approach allows to eliminate both the contribute due to the channel and aberrations due to the glass slide and the liquid that contains the spermatozoa. Since in microfluidic channels

the flat area surrounding the channel is very wide (compared to the channel area), the object wavefront can be used to obtain a self-reference interferometry, as it has been recently demonstrated by Jang et al. (50). The Jang's set-up allows to create an interferogram between the original object wavefront and an its mirror replica. This replica was obtained by a fine optical adjustment and alignment of a microscope objective added into an additional arm of the set-up. The two wavefronts interfere in such a way that a flat area is superimposed to the area occupied by the microfluidic channel with the biological specimen. This approach has been demonstrated to be valid for reconstructing quantitatively the phase distribution of different specimens. Nevertheless, the method described in (50) requires both an appropriate set-up and 2D weighted polynomial fitting. Taking advantage of the possibility offered by DH to numerically manage the reconstructed complex wavefronts, a novel and full numerical approach can be adopted to get QPMs (51), (52). The method is based on the generation of a numerical replica of the original complex wavefield. The replica is digitally shifted and the corresponding phase is subtracted from the original wavefront in order to obtain the desired QPM. Our approach can be explained as a wavefront folding which allows to superimpose the portion corresponding to a flat region on the region in which the object under investigation lies. Compared to the method reported in (50), that can be considered a true self-reference optical set-up, in our approach the replica is obtained numerically and for this reason the expression "digital self-referencing" has been adopted. Moreover a standard Mach-Zehnder set-up has been used, whereas in (50) a Michelson configuration was adopted. The effectiveness of the our method has been proved for different objects.

DHM has been used for characterization of Nuclear Vacuoles on human sperm cells. Nuclear vacuoles have been described as a crater defect in the spermatozoa of stallion, as a crater defect , a pouch formation, a diadem defect or a nuclear sperm defect in bull spermatozoa, and as a crater defect or a pouch formation in boar spermatozoa. The defect is believed to originate during spermiogenesis as vacuoles have been found in both early and late spermatids. Nuclear vacuoles were shown by electron microscopy to be narrow-mouthed invaginations of the nuclear membrane into the nucleoplasm. The

appearance of these 'nuclear pouches' in bull spermatozoa forming a string at the site of the acrosome postacrosomal sheath junction gave rise to the name 'diadem defect'. The predominant locations of the vacuoles are the apical region and the acrosome-postacrosomal sheath junction but they have also been found throughout the sperm head. We have used Digital Holographic Microscopy as a novel approach for a more advanced morphological analysis of human spermatozoa. Quantitative 3D reconstructions of sperm head, both normal and anomalous, have been studied and an unexpected structure of the post-acrosomal region of the head has been highlighted. Moreover, employing a microfluidic-system on unstained spermatozoa in their natural physiological surroundings has been analysed (49).

Part of the research activities has been carried out at the Microgravity Research Center – Université Libre de Bruxelles, supervised by Prof. Frank Dubois. The activities has been devoted to the development of an algorithm for the detection and the tracking of biological particle by means of a Partially Coherent DHM, setup developed by the research group of Prof. Dubois. The detection and the tracking of micrometric particles, such as bacteria, cells or marine microorganism, is an important task for the evaluation of biological parameters. In order to evaluate the vitality of sperm cells, special relevancy is associated to the knowledge related to the motility, i.e. curvilinear and linear velocity, wobble etc. The approach described in this proceeding, making use of a partially spatial coherent source, has the major advantage of reducing drastically the speckle noise, thus providing an higher image quality (31). A set of holograms relatives of a particle flowing in a microchannel has been acquired and an algorithm for the detecting and the tracking of the particle has been developed. The described approach has been tested on several fluxes. The coordinates of the particle obtained by the detecting procedure are reasonable and consistent with the expected values. Subsequently the same technique has been applied, after several adjustment, to a single Paramecium moving in a free space. The dimension of this objects is about tenth of μm. Subsequently the procedure have been applied for the tracking of multiple particles, where the procedure applied to the whole phase map failed making confusion between the different particles. Thanks to a proximity criterion this problem has been a solved. Finally the tracking procedure

has been successfully applied to the case of a human sperm cell, presenting a “bent tail” anomaly.

In the end, DHM has been successfully applied to the analysis of both human and animal sperm cell, compatibly with micro-featured structures and a full description of the biological sample has been retrieved: static informations such as shape and thickness, and dynamical properties, such as velocity, linearity, wobble etc.

8. BIBLIOGRAPHY

1. *The origins and the future of microfluidics.* **Whitesides, G. M.** 2006, Nature, Vol. 442, p. 368-373.

2. *Cells on Chips.* **J. El-Ali et al.** 2006, Nature, Vol. 442, p. 403-411.

3. *Microfluidic diagnostictechnologies for global public health.* **P. Yager et al.** 2006, Nature, Vol. 442, p. 7101.

4. **Franken, R. D.** The clinical significance of sperm zone pellucida binding. *Front Biosci.* 1998, Vol. 3, p. 247-253.

5. *The spatial variation of the refractive index in biological cells.* **J. Beuthan et. al.** 1996, Phys. Med. Biol., Vol. 41, p. 369.

6. *Some variability factors in the cytomorphological analysis of frozen bull semen.* **A. Galli, L. Paloschi and F. Pizzi.** 1989, Andrologia, Vol. 21, p. 120-126.

7. *Flow cytometric sexing of mammalian sperm.* **Garner, D. L.** 2006, Theriogenology, Vol. 65, p. 943-957.

8. *Atomic force microscopy: A powerful tool for high-resolution imaging of spermatozoa.* **S. Kumar, K. Chaudhury, P. Sen and S. K. Guha.** 2005, J. Nanobiotechnol., Vol. 3, p. 3-9.

9. *The natural subcellular surface structure of the bovine sperm cell.* **M. J. Allen, E. M. Bradbury and R. Balhorn.** 1995, J. Struct. Biol., Vol. 114, p. 197-208.

10. *A microfluidic shadow imaging system for the study of the nematode Caenorhabditis elegans in space.* **D. Lange et al.** 2005, Sensors Actuators B, Vol. 107, p. 904-914.

11. *Digital in-line holographic microscopy.* **J. Garcia-Sucerquia et al.** 2006, Appl. Opt., Vol. 45, p. 863-850.

12. *Developing optofluidic technology through the fusion of microfluidics and optics.* **D. Psaltis et al.** 2006, Nature, Vol. 442, p. 381-386.

13. **W. Lauterborn, T. Kurz, and M. Wiesenfeldt.** *Coherent Optics.* s.l. : Springer, 1993.

14. **J. W. Goodman** *Introduction to Fourier Optics.* s.l. : McGraw-Hill, 1996.

15. **Gabor, D.** A new microscopic principle. *Nature.* 1948, Vol. 161, p. 777-778.

16. **E. N. Leith and I. Upatnieks** Wavefront reconstruction with diffused illumination and three-dimensional objects. *Journal of the Optical Society of America.* 1964, Vol. 54, p. 1295–301.

17. **T. Kreis,** *Holographic Interferometry.* Berlin : Akadamie, 1996.

18. **Y.I. Ostrovsky, M.M. Butosov, G. V. Ostrovskaja.** *Interferometry by Holography.* s.l. : Springer, 1981.

19. Phase-shifting holographic interferometry. [aut. libro] K. Creath. *Holographic Interferometry.* Berlin : Springer, 1994.

20. *Direct recording of holograms by a CCD target and numerical reconstruction.* **U. Shnars et al.** s.l. : Applied Optics:, Vol. 33, p. 179-181.

21. **L. P.Merzlyakova and N. S Yaroslavskii** *Methods of Holography Digital Holography.* New York : Consultants Bureau, 1980.

22. **E. O. Brigham,** *The Fast Fourier Transform.* s.l. : Englewood Cliffs, NJ; Prentice-Hall, 1974.

23. *Digital and optical reconstruction of images from suboptical diffraction patterns.* **T. H. Mittra and R. Demetrakopoulos** 1974, Appl.Opt., Vol. 13, p. 665–70.

24. *Digital recording and numerical reconstruction of lensless Fourier holograms in optical metrology.* **C. Wagner, S. Seebacher, W. Osten and W. Juptner.** 1999, Appl. Opt., Vol. 38, p. 4812–20.

25. *Suppression of the dc term in digital holography.* **T. Juptner and W. Kreis** 2357-60, 1997, Opt. Eng., Vol. 36.

26. *Fourier optics described by operator algebra.* **M. Shamir and J. Nazarathy** 1980, J. of the Opt. Soc. of Am., Vol. 70, p. 150-159.

27. *Digital holographic microscopy with reduces spatial coherence for three domensionale particle plow analysis.* **F. Dubois, N. Callens, C Yourassowsky, M. Hoyos, P. Kurowsky and O. Monnom.** 2006, Appl. Opt, Vol. 45, p. 864-871.

28. **P. Ferraro, S. DeNicola, A. Finizio, G. Coppola, S. Grilli, C. Magro, and G. Pierattini.** 2003, Appl. Phys. Lett., Vol. 42, p. 1936.

29. *Quantitative phase-contrast microscopy by a lateral shear approach to digital holographic image reconstruction.* **P. Ferraro, D. Alfieri, S. De Nicola, L. De Petrocellis, A. Finizio and. G. Pierattini.** 2006, Opt. Lett., Vol. 31, p. 1406-1409.

30. *Focus plane detection criteria in digital holography microscopy by amplitude analysis.* **F. Dubois, C. Schockaert, N. Callens and C. Yourassowsky.** 2006, Optics Express, Vol. 14, p. 5895-5908.

31. *Partial satial choerence effects in digital holographic microscopy witha laser source.* **F. Dubois, M. L. Novella Requena, C. Minetti, O Monnom and E. Istasse.** 2004, Appl. Opt., Vol. 43, p. 1131-1139.

32. **F. Dubois, C Yourassowky, N. Callens, C. Minetti, P. Queeckers, T. Podgorski ans A. Brandenbrurger.** *Coherent Light Microscopy - Chapter 2 Digital Holographic Microscopy working with a Partially Spatial Coherent Source.* s.l. : Springer , 2011.

33. *Image formation in phase shifting Digital Holography and application to microscopy.* **I. Yamaguchi, J. Kato, S. Otha and J. Mizuno.** 2001, Appl. Opt., p. 6177-6186.

34. *Iterative algorithm with a constraint condition for numerical reconstruction of a three-dimensional object from its hologram.* **L. Cai and L. Yu** J. Opt. Soc. Am. A, Vol. 18, p. 1033-1045.

35. *Fabrication of microfluidic systems in poly(dimethylsiloxane).* **J. C. McDonald, D. C. Duffy, J. R. Anderson, D. T. Chiu, H. Wu, O. J. A. Schueller and G. M. Whitesides.** 2000, Electrophoresis, Vol. 21, p. 27-40.

36. **E. S. E. Hafez,** *Reproduction in Farm Animals.* Philadelphia : Lea & Febiger, 1987.

37. *Expression of mammalian spermatozoal nucleoproteins.* **J. P. Dadoune,** 2003, Microsc. Res. Tech., Vol. 61, p. 56–75.

38. **K. Dale and B. Elder** *In-vitro fertilization, 3rd Edition.* s.l. : Cambridge University Press, 2011.

39. **G. Gerton,** *Function of the sperm acrosome. In: Fertilization.* s.l. : D. Hardy for San Diego Academic Press, 2002.

40. *Organization and modifications of sperm acrosomal molecules during spermatogenesis and epididymal maturation.* **K. Toshimori and K. Yoshinaga** 2003, Microsc. Res. Tech., Vol. 61, p. 39-45.

41. *Developmental expression and possible role of perinuclear theca proteins in mammalian spermatozoa.* **R. J. Oko,** 1995, Reprod. Fertil. Dev., Vol. 7, p. 777-797.

42. *Predictive value of abnormal sperm morphology in vitro fertilization.* **T. F. Kruger, A. A. Acosta, K. F. Simmons, R. J. Swanson, J. F. Matta and S. Oehninger S.** 1998, Fertil. Steril., Vol. 49, p. 112-117.

43. *Pregnancies after intracytoplasmic injection of single spermatozoon into an oocyte.* **G. Palermo, H. Joris, P. Devroey, A. C. Van Steirteghem.** 1992, Lancet., Vol. 370, p. 17-18.

44. **A. D. Oko and R. J. Barth** *Abnormal morphology of bovine spermatozoa.* s.l. : Wiley-Blackwell, 1991.

45. *Digital holographic microscopy: A noninvasive contrast imaging technique allowing quantitative visualization of living cells with subwavelength axial accuracy.* **P. Marquet, B. Rappaz, P. J. Magistretti, E. Cuche, Y. Emery, T. Colomb, and C. Depeursinge.** 2005, Opt. Lett., Vol. 30, p. 468-470.

46. *The natural subcellular surface structure of the bovine sperm cell.* **M. J. Allen, E. M. Bradbury, and R. Balhorn.** 1995, J. Struct. Biol., Vol. 114, p. 197-208.

47. F. A.: Qualità seminale e fertilità. *Informatore Zootecnico, zootecnia e veterinaria.* 1987.

48. *Quantitative Label-Free Animal Sperm Imaging by Means of Digital Holographic Microscopy",.* **G. Di Caprio, M. Gioffré, N. Saffioti, S. Grilli, P. Ferraro, R. Puglisi, D. Balduzzi, A. Galli and G. Coppola.** 2010, IEEE, Journal of Selected Topics in Quantum Electronics, special issue in Biophotonics, Vol. 43, p. 833-840.

49. *Digital holographic microscopy for the evaluation of human spermatozoon structure.* **G. Di Caprio, G. Coppola, G. Coppola, M. Wilding, P. Ferraro, G. Esposito, L. Di Matteo, R. Dale and B. Dale.** 2011, Submitted to Reproductive BioMedicine Online.

50. *Self-reference quantitative phase microscopy for microfluidic devices.* **J. Jang, C. Yun Bae, J. Park and J. C. Ye.** 2010, Opt. Lett., Vol. 35, p. 514-516.

51. *Digital self-referencing quantitative phase microscopy by wavefront folding in holographic image reconstruction.* **G. Coppola, G. Di Caprio, M. Gioffré, R. Puglisi, D. Balduzzi, A. Galli, L. Miccio, M. Paturzo, S. Grilli, A. Finizio and P. Ferraro.** 2010, Optics Letters, Vol. 35, p. 3390-3392.

52. **L. Miccio, S. Grilli, M. Paturzo, A. Finizio, G. Di Caprio, G. Coppola, P. Ferraro, R. Puglisi, D. Balduzzi and A. Galli.** Quantitative Phase Contrast in holographic microscopy trough the numerical manipulation of the retrieved wavefronts. *Coherent Light Microscopy.* s.l. : Ed. Springer, 2010.

53. **E. S. E. Hafez***: Reproduction in farm animals.* Philadelphia : Lea & Febiger, 1987.